IOP PUBLISHING JOURNAL OF PHYSICS D: APPLIED PHYSICS

J. Phys. D: Appl. Phys. **42** (2009) 243001 (21pp) doi:10.1088/0022-3727/42/24/243001

TOPICAL REVIEW

Advances in neutron radiography and tomography

M Strobl[1,2,4], I Manke[1,3], N Kardjilov[1], A Hilger[1], M Dawson[1] and J Banhart[1,3]

[1] Helmholtz-Centre Berlin for Materials and Energy (Hahn-Meitner Institute), Hahn-Meitner-Platz, 14109 Berlin, Germany
[2] Ruprecht-Karls-University Heidelberg, Physikalisch-Chemisches Institut, Im Neuenheimer Feld 229, 69120 Heidelberg, Germany
[3] Technische Universität Berlin, Institute of Materials Science and Technology, Hardenbergstr. 36, 10623 Berlin, Germany

E-mail: strobl@helmholtz-berlin.de

Received 3 March 2008, in final form 5 August 2009
Published 30 November 2009
Online at stacks.iop.org/JPhysD/42/243001

Abstract
Neutron imaging can provide two- or three-dimensional, spatially resolved images of the internal structure of bulk samples that are not accessible by other techniques, making it a unique tool with many potential applications. The method is now well established and is available at neutron sources worldwide. This review will give a survey of the technique of neutron imaging with a special focus on neutron tomography; the basics of the method as well as the technology of instrumentation will be outlined, and the techniques will be illustrated by representative applications. While the first part of the paper focuses on conventional attenuation contrast imaging, the second part reviews and critically assesses recent methodical developments.

(Some figures in this article are in colour only in the electronic version)

1. Introduction

Neutron imaging has a history spanning more than seven decades [1] though it was only about 40 years ago that it experienced a surge in interest [2, 3] and slowly began to advance into a reliable and applicable non-destructive testing method. The increased rate of development in recent times can be explained by the rapid progress in digital image recording [4] that started some 10 years ago. Although early digital imaging systems provided poorer resolution than the previously used films, they boosted development since the simplifications associated with the recording, handling and treatment of digital data [4, 5] enabled tomography (rather than just radiography) to be carried out on a routine basis. This implementation led directly to the development of the state-of-the-art neutron imaging facilities at today's major reactor and spallation neutron sources [6]. Currently, neutron imaging is part of the instrumentation programme at many large-scale neutron facilities around the world (see table 1), making it more accessible more easily for a larger number of scientific applications.

2. Fundamentals

That neutrons are a unique probe not only for diffraction and scattering studies but also for imaging is inherently connected to the fact that they have zero net charge. Consequently, unlike x-rays, neutrons do not interact (or at most interact negligibly) with the electronic charge of the electrons. Instead, they interact strongly with the atomic nucleus (figure 1). Hence, while for x-rays the interaction cross-section increases with the number of electrons (i.e. with atomic number), no such systematic correlation can be found for the strong interaction forces between neutrons and nuclei. As neutrons directly probe nuclei, they give strong contrast for some elements that are

[4] Author to whom any correspondence should be addressed.

Table 1. International selection of major neutron imaging facilities and their host institutions (alphabetic).

Institution	Facility	Location	Instrument
Atomic Energy Research Institute	BNC	Budapest, Hungary	NRAD
Atominstitut der österreichischen Universitäten	ATI	Vienna, Austria	Neutronenradiographie
Forschungszentrum Geesthacht	FRG1	Geesthacht, Germany	GENRA-3
Helmholtz-Centre Berlin (Hahn-Meitner-Institut)	BER-2	Berlin, Germany	CONRAD 1&2
Institute Laue-Langevin	ILL	Grenoble, France	NEUTROGRAPH[a]
Japan Atomic Energy Res. Institute	JRR-3M	Tokaimura, Japan	
Korean Atomic Energy Res. Inst.	HANARO	Daejeon, Korea	NRF
Laboratoire Leon Brillouin	Orphee	Gif-sur-Yvette, France	Neutronographie
National Institute of Standards	NCNR	Gaithersburg, USA	BT2 NIF
Nuclear Energy Corp. South Africa	SAFARI	Pelindaba, South Afr.	NRAD
Paul-Scherrer-Institut	SINQ	Villigen, Switzerland	NEUTRA / ICON
Technische Universität München	FRM-2	Garching, Germany	ANTARES / NECTAR

[a] Not available at the moment.

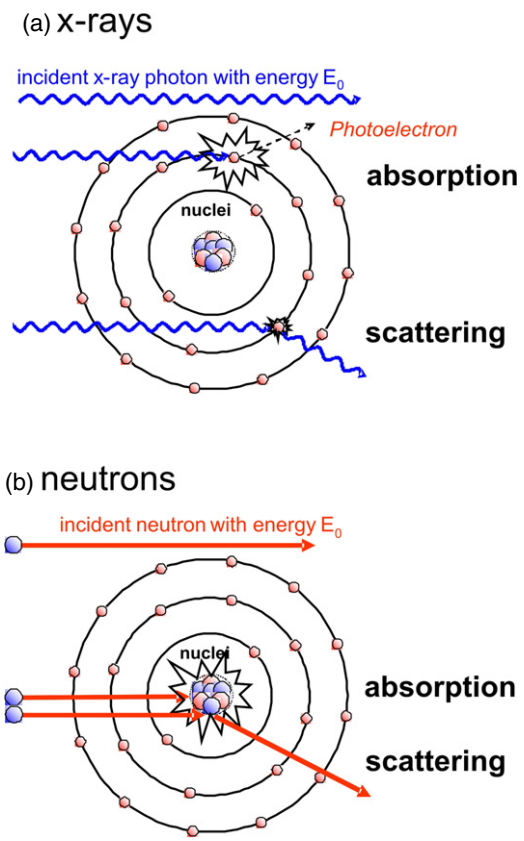

Figure 1. Interaction of matter with (*a*) x-rays and (*b*) neutrons.

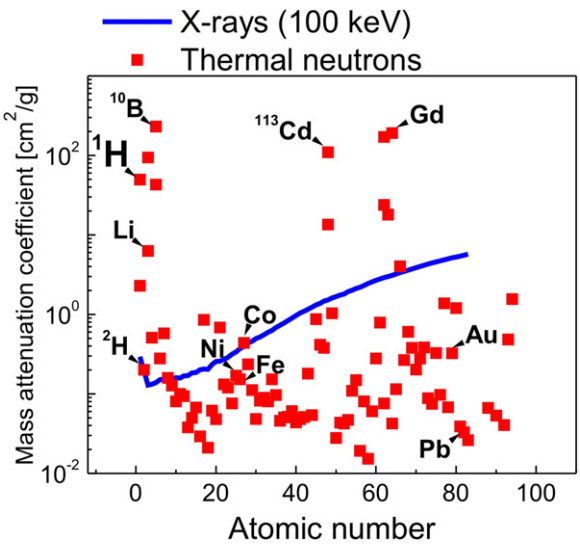

Figure 2. Mass attenuation coefficients for thermal neutrons and 100 keV x-rays for the elements (natural isotopical mixture unless stated differently). (Reprinted with permission from [10]. Copyright 2008, University of Oxford Press.)

close to one another in the periodic table, and are even able to distinguish between different isotopes. Furthermore, several light elements (notably hydrogen) attenuate strongly, while layers of many metals that are several centimetres thick can be penetrated; for example, the heavy element lead is used for shielding x-rays, but could be deemed a window material for neutrons. Figure 2 compares the mass attenuation coefficients of thermal neutrons and 100 keV x-rays (a typical energy used in imaging) and clearly demonstrates the complementarity of neutron and x-ray imaging for a broad range of materials. An important and industrially relevant example is the ability of neutrons to detect even small amounts of hydrogen-containing materials such as water, many synthetics (e.g. lubricants, glues, etc) or plastics contained within metals; in contrast, x-rays are better suited to identifying small metallic regions inside synthetic matrices.

Another factor worth considering alongside the relative penetrability of different materials with neutrons and x-rays is the spatial resolution attainable and the volume of the sample that can be imaged. Though the penetration depths achieved with thermal neutrons for a broad range of important industrial materials such as metals are significantly higher (around an order of magnitude) compared with standard x-ray energies of several tens or hundred kiloelectronvolts, the best spatial resolution available with neutrons is at least one order of magnitude lower. As a consequence of this, along with the fact that neutron beams generally have a larger cross-section than high intensity synchrotron x-ray beams, neutron (high-resolution x-ray) tomography is suited to investigating sample volumes of several cubic centimetres (millimetres).

Material attenuation coefficients (cf figure 2) are energy-dependent for both neutrons and x-rays. However, for many applications the energy range of neutrons used for scattering experiments, i.e. thermal and cold neutrons (around 25 meV

and 4 meV, respectively) for which the wavelengths[5] match the inter-atomic spacing of crystal lattices (of the order of Å, 10^{-10} m), is the best compromise between penetration depth and achievable contrast between different materials. For some applications, which this paper will not discuss further, higher energy neutrons are demanded [8, 9].

Neutron tomography, like other tomographic techniques, provides three-dimensional spatially resolved images (i.e. volumetric data), which generally display the attenuation coefficient distribution in the sample volume [10]. The volumes are reconstructed from a set of projection images (radiographs) recorded at different equidistant angles (typically several hundred) spread 180° around the sample. The projection images are formed according to the exponential Beer–Lambert attenuation law:

$$I(x, y, E) = I_0(x, y, E) \cdot \mathrm{e}^{-\int_{\mathrm{path}} \mu(x,y,z,E)\cdot \mathrm{d}s}, \tag{1}$$

where I_0 and I are the incident and attenuated intensities, respectively, μ is the linear attenuation coefficient of the material (combining the interaction cross-section and nuclear density) and s is the path length through the sample.

2.1. Reconstruction of tomographic images

The underlying theory for reconstruction was formulated at the beginning of the last century [11] and advantage can be taken of the Fourier slice theorem [12, 13] by applying the filtered back projection (FBP) algorithm. However, in most cases some simplifying approximations are used in order to make the algorithm more straightforward. First, the beam is considered to be parallel (i.e. perfectly collimated), since this allows the reconstruction to be applied slice by slice. Second, interactions outside the sample and scattered neutrons are not taken into account. Third, the beam is considered mono-energetic (even when a polychromatic beam is used), such that the energy dependence of the material attenuation coefficients is neglected. Taking this into account, the so-called Radon transformation [10, 11] for the one-dimensional projections $P_\theta(t)$ of single slices at angles θ can be formulated, according to equation (1), as

$$\begin{aligned} P_\theta(t) &= -\ln \frac{I_\theta(t)}{I_0(t)} = \int_{\mathrm{ray}(\theta,t)} \mu(x, y) \cdot \mathrm{d}s \\ &= \int_{-\infty}^{\infty}\int_{-\infty}^{\infty} \delta_D(x\,\cos\theta + y \sin\theta - t) \\ &\quad \times \mu(x, y) \cdot \mathrm{d}x\,\mathrm{d}y, \end{aligned} \tag{2}$$

where $t = x\cos\theta + y\sin\theta$ and is perpendicular to the rotation axis. From multiple one-dimensional projection functions, $P_\theta(t)$, the two-dimensional function $\mu(x, y)$ can be reconstructed by means of the Fourier slice theorem. It states that the one-dimensional Fourier transform $P_\theta(\omega)$ of the projections $P_\theta(t)$ of the two-dimensional function $\mu(x, y)$ is equal to the two-dimensional Fourier transform $S(u, v)$ of the slice $\mu(x, y)$. Consequently, an infinite number of projections will fill the whole Fourier space and enable a perfect reconstruction of $\mu(x, y)$ by the back transformation

$$\begin{aligned} \mu(x, y) &= \int_{-\infty}^{\infty}\int_{-\infty}^{\infty} S(u, v) \cdot \mathrm{e}^{2\pi\mathrm{i}(ux+vy)} \cdot \mathrm{d}u\,\mathrm{d}v \\ &= \int_0^{\pi}\int_0^{\infty}\left(\int_{-\infty}^{\infty} P_\theta(t) \cdot \mathrm{e}^{-2\pi\mathrm{i}\omega t} \cdot \mathrm{d}t\right) \\ &\quad \times \mathrm{e}^{2\pi\mathrm{i}(x\,\cos\theta + y\,\sin\theta)} \cdot |\omega| \cdot \mathrm{d}\omega\,\mathrm{d}\theta, \end{aligned} \tag{3}$$

where $|\omega|$ results from the transformation into polar coordinates (u, v). The relation $S(\omega, \theta + \pi) = S(-\omega, \theta)$ is responsible for allowing rotation to be restricted to 180°; the integral can be performed to π instead of 2π by replacing ω with $|\omega|$. The function

$$Q_\theta(t) = \int_0^{\infty} P_\theta(\omega) \cdot \mathrm{e}^{2\pi\mathrm{i}(x\,\cos\theta + y\,\sin\theta)} |\omega| \cdot \mathrm{d}\omega \tag{4}$$

is then called a filtered projection where $|\omega|$ can be considered to be a ramp filter. However, real data consist of just a discrete number of projections consisting of discrete data points related to the spatial resolution; they do not fill the Fourier space. Thus various filter functions are often carefully selected to either enhance or suppress certain frequencies and thereby to improve the quality of the resulting reconstructed images. The highest resolvable frequency in the reconstruction is given by the Nyquist theorem:

$$\omega_{\max} = \pi/2\Delta t, \tag{5}$$

where Δt is the spatial resolution in each projection. The integration can be limited to this value. Instead of multiplication in the frequency domain, a convolution in the space domain can be employed, which is reduced by the discrete measured values to a fast computed summation. Accordingly an optimum value can be found for the relation between the number of projections, M, and the number of points per projection, N, from

$$\frac{M}{N} = \frac{\pi}{2}. \tag{6}$$

Several other approaches exist for reconstructing the volume of a sample [14–17] and these must be employed when the above approximations do not hold, e.g. cone-beam geometry, limited angular access, incomplete data, extremely noisy data, etc.

Various influences on the measured signal that are not accounted for in the given theory for reconstruction (for example, excessive noise in the projection data) can cause severe image artefacts in the reconstructed images and volumes.

2.2. Image processing and artefacts

The presence and production of artefacts in a real measurement system have to be considered carefully and should be avoided (preferable) and corrected as accurately as possible prior to tomographic reconstruction. Recorded images are contaminated by several factors: electronic noise in the detector

[5] Due to the wave–particle dualism a specific kinetic energy E of neutrons corresponds not only to a velocity v of the particles but to a wavelength λ corresponding to $\lambda = h/mv$ where h is the Planck constant and m the mass of the neutron [7].

system, spatial and temporal variations in the incident beam intensity, inhomogeneities in the scintillator and detector and white spots caused by fast neutrons and gamma radiation. The first three effects can be corrected by normalization with respect to measured background (dark field) and beam intensity distribution (flat field) measurements, respectively. White spots, which increase in number with increasing exposure time, can be eliminated or marginalized by filter operations; measuring several images for each projection allows median or erosion (low-pass) filters to be applied. Other artefacts may be caused by scattering, refraction, spectral effects induced by the sample (beam hardening), and the correction of these is non-trivial and remains a challenge. Artefacts exhibit themselves in reconstructions as rings, lines and star-bursts (among others) and can hinder correct interpretation and quantification. Further points worth bearing in mind regarding tomographic scans are that the sample must be stable, the sample must be smaller than the beam cross-section at any projection angle and the rotation axis must be aligned correctly with respect to the slice by slice reconstruction procedure described above. Due to the beam geometry—a perfect parallel beam cannot be provided—scans in the range of 360° instead of 180° can help to improve image quality (in particular for large samples). Further, the application of a cone-beam reconstruction algorithm can be considered for improved reconstruction quality.

3. Instrumentation

The two main criteria in neutron imaging applications are usually the temporal resolution—limited by exposure and read-out time—and spatial resolution; these two quantities are strongly interdependent. They are influenced and limited by the three main components of a neutron imaging facility: the source, the collimation (or flight path) and the detector. A typical setup for tomographic imaging is shown in figure 3. Other necessary components such as shielding and sample stages will not be dealt with here as they are considered to be of practical and technical rather than of methodical interest.

3.1. Source

Most of the existing neutron imaging instruments are located at continuous sources, typically research reactors, i.e. stationary large-scale facilities [6][6] (see table 1). Even the largest of these sources are inherently flux-limited shown by the fact that the flux of these sources—unlike that of synchrotron x-ray sources—has hardly changed over the past few decades and hence impose principal limitations on neutron imaging [10]. With the advent of powerful spallation sources such as the SNS (USA) and the source at J-Parc (Japan), there are efforts to exploit some of the advantages of these facilities for imaging as well. No such instruments exist at present, but some hints for the potential of instruments utilizing a time-structured beam can be found in section 5. The flux densities at the sample position available nowadays range from

[6] For radiographic applications also smaller [18] and even portable sources [10, 18] are used.

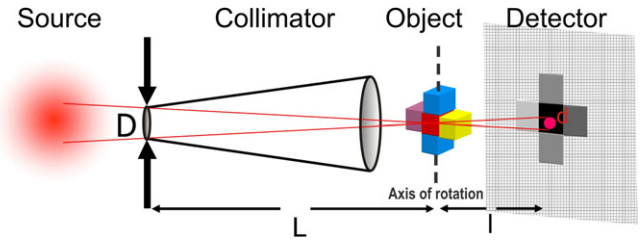

Figure 3. Typical geometry of a neutron imaging instrument.

$10^6\,\mathrm{cm^{-2}\,s^{-1}}$ to about $10^9\,\mathrm{cm^{-2}\,s^{-1}}$ in modern instruments. Fission or spallation neutrons are generated with energies of a few megaelectronvolts, but are slowed down by interaction with a moderator to lower energies in order to fit the needs of scattering and imaging experiments. The moderator is usually water or heavy water for thermal neutrons and liquid deuterium cooled to several kelvins for cold neutrons. The corresponding neutron wavelengths range between 1 Å and approximately 10 Å. In general, neutron extraction from the source should avoid a direct view on the core because this leads to an admixture of epithermal neutrons, fast neutrons and γ rays to the beam, all of which can be considered as undesirable background radiation. The use of neutron guides for the purpose of beam extraction has advantages as well as disadvantages. On the one hand, they offer a (nearly) lossless transport of neutrons to the experiment, which might be located at a large distance from the source. Furthermore, by employing a curved guide, the aforementioned background can be reduced efficiently. On the other hand, the guide transports neutrons with a finite divergence given by the critical angle of reflection from the guide walls, which is also wavelength-dependent [4, 19]. This has several consequences for the resulting beam cross-section and its spectral and flux homogeneity (as will be discussed in the following section). In addition, a specific cut-off wavelength on the short wavelength side is defined by the coating and curvature of the guide, and the limited divergence of the transported beam is a limiting factor for the field of view. However, new developments such as ballistic guides and so-called high-m (m is the factor by which the total reflection angle is increased as compared with natural Ni) supermirror coatings might be able to solve such problems.

3.2. Beam formation and collimation

A point source is generally considered to be the optimum geometry for neutron imaging and in most instruments this is achieved simply by a small pinhole with a diameter D and a long pinhole-to-sample distance L (figure 3). For imaging purposes, collimation is most usefully characterized by the collimation ratio L/D and this ratio limits the geometrical resolution, d, at a certain sample–detector distance, l, as given by

$$d = l \cdot (L/D)^{-1}. \tag{7}$$

A well-collimated beam (i.e. low divergence) is thus a fundamental pre-requisite for achieving high spatial resolution. At the same time, the beam cross-section increases along the (often evacuated) flight path due to the divergence of the

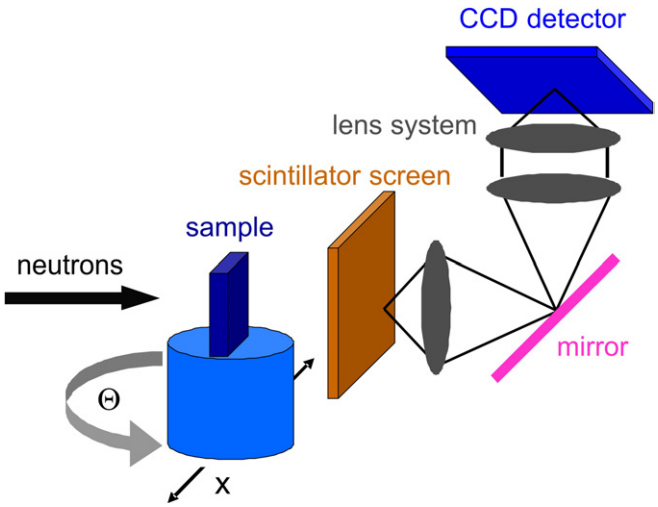

Figure 4. Typical tomography setup.

beam emanating from the point source. If this divergence is wavelength-dependent due to an upstream neutron guide, the beam cross-section will increase differently for different neutron energies and the beam at the sample position will exhibit spectral inhomogeneities (i.e. the wavelength distribution varies over the field of view). Devices such as focusing guides have been proposed and tested in order to increase the beam divergence beyond that produced by the coating of the neutron guide [20]. Currently, L/D values of several hundred to a thousand and beam cross-sections of 10×10 to $40 \times 40\,\mathrm{cm}^2$ are available. If a sample is bigger than the available beam cross-section, exposure in a scanning mode has proved to be efficient for radiography as well as tomography [21].

3.3. Detection

As already mentioned above, digital imaging detectors have been the key factor driving the development of modern neutron imaging instruments. These are necessary for tomographic measurements in order to ensure consistent object–detector alignment and also for efficient data handling. Other advantages of digital imaging detectors are their higher time resolution and larger linear dynamic range. In some special radiographic applications films, track edge foils or imaging plates may still be used—mostly for their superior spatial resolution. In most cases, however, scintillator screens in conjunction with either charge-coupled device (CCD) cameras or sometimes flat amorphous-Si detectors are utilized (see figure 4), both of which can be read out digitally. Amorphous-Si flat panels require shorter exposure times and provide faster continuous read-out [22–25], while state-of-the-art scintillator CCD combinations [4, 26] are superior concerning dynamic range and signal-to-noise and so give improved image quality. Unlike amorphous silicon, CCD chips cannot be placed directly in a neutron beam, since they would suffer radiation damage. CCD cameras are therefore placed in a light-tight box in which the light from the scintillator placed at the front window is deflected out of the neutron beam direction and towards the optics of the CCD camera by a mirror. The detector system has a pronounced influence on the image quality achieved and various detector components have to be optimized; both the optical lens system and the scintillator screen are a focus of ongoing improvements. It is only recently that the detector resolution fell below the long-standing $100\,\mu$m limit, and it is now approaching a few tens of micrometres [27–29].

Conventional scintillators for neutron imaging (which convert neutrons into light) are crystalline ^{6}LiF/ZnS : Ag screens with thicknesses of between 0.2 and 0.03 mm. The thickness is crucial for resolution and efficiency (related to neutron capture probability, light output efficiency, self-shielding and dissipation lengths of the ^{6}Li-neutron reaction products). Silver doping shifts the scintillation light emission wavelength to the spectral range of the maximum efficiency of the CCDs (blue–green, around 450 nm). However, GADOX (gadoliniumoxisulfite) scintillators used for x-ray imaging [10] have recently been rediscovered for neutron imaging. Gadolinium has a higher interaction cross-section than lithium and so these scintillators can be thinner, enabling high spatial resolution, in particular when using cold neutrons for which the efficiency drawback is less severe.

Up to the present, the CCDs used for standard applications are Peltier-cooled chips of several square centimetres area consisting of 1024×1024 to 2048×2048 (and sometimes more) pixels. For short exposure and read-out for real-time or stroboscopic applications, CMOS cameras combined with image amplifiers can also be utilized. These enable read-out times of the order of milliseconds and, when using triggered amplifiers, exposure times down to several nanoseconds.

A new development in the field of detector systems for neutron imaging is the application of micro channel plates (MCP). These exploit the ^{10}B(n,α)^{7}Li capture conversion process on their active inner surface. These devices have provided promising first results concerning very high spatial ($<20\,\mu$m) and temporal ($<\mu$s) resolution [30].

3.4. Fundamental considerations and limitations

Even for technically optimized neutron imaging setups, a trade-off has to be found between exposure time and spatial resolution based on the needs of the experiment. To increase the geometric resolution in a radiogram, (for example) by a factor of two, the pinhole aperture D also has to be decreased by a factor of two, implying a flux density reduction to one-fourth the original value. Additionally, the 'effective' pixel size has to be reduced correspondingly. In this case, the number of counts per resolved detector area unit (pixel) could be as low as one-sixteenth of the original value. Many of the world-leading neutron imaging instruments possess a pinhole changer for the purpose of flexible adjustment of L/D, but in all cases increasing the spatial resolution is only possible at the price of significantly longer acquisition times. For high-resolution tomographic investigations, acquisition times must be increased yet again, since the number of projection angles has to be increased to resolve the third dimension with the same gain of resolution. Typical exposure times for single images range between seconds and several minutes in modern instruments.

The total number of pixels available is fixed by the CCD detector used and thus provides a physical limit on the attainable pixel resolution, since it is necessary to consider also the field of view required to image the sample. The total field of view scales directly with the effective pixel size.

The choice of neutron energy spectrum used usually depends on the composition and size of the sample under investigation; in general, cold neutrons provide higher contrast between different elements, but thermal neutrons can penetrate thicker samples. Sample activation is another issue. Depending on the materials involved, the neutron energy, the flux density at the sample position and the exposure time, the sample may become radioactively activated. The level of this activation and the time the radiation will take to decay have to be considered carefully, and it is always advisable to calculate this in advance.

In instances where the exposure time is kept low (to increase temporal resolution or to avoid activation, for example) or when the signal is low due to strong attenuation or the available flux density, the achievable signal-to-noise ratio is critical for the feasibility of the experiment. As previously mentioned, noisy data are difficult to interpret and quantify and produce artefacts in tomographic reconstructions.

4. Applications

The scope of neutron imaging applications is wide and difficult to summarize while claiming completeness. Applications range from non-destructive testing of industrial components and support in research and development to scientific investigations in various fields such as biology, geology, archaeology, history, materials science and physics [31–53]. In addition, the potential of this relatively young technique is still far from being fully explored and exploited and, as a result, new applications are constantly emerging. In the following, some of the more prominent and typical applications of neutron imaging techniques will be given, ranging from time-resolved radiography on fuel cells to volumetric imaging of historical objects. The reasons why neutron imaging has been chosen in these cases as well as the basic issues of the investigations will be provided in as much detail as possible.

4.1. Fuel cells

Fuel cells are of particular importance for the development of future efficient energy conversion systems in mobile (e.g. cars) and stationary (e.g. power plants) units. One of the most promising approaches is the polymer electrolyte membrane fuel cell (PEMFC). In an electrolytic process the reactant gases H_2 and O_2, which are supplied to the cathodic and anodic side of the cell, respectively, form water and deliver electrical energy [54, 55]. The product 'liquid water' is needed to a certain extent to wet the membrane in order to support the performance of the cell, but excessive water agglomerations have to be removed through flow-field channels in order to keep the gas supply through these channels at a stable level. Besides being part of the reaction chain, water also has a considerable impact on cell durability as it contributes to the corrosion of gas diffusion media, electrodes, the catalyst layers and the membrane. Efficient water management is thus a key issue not only for the efficiency, but also for the lifetime of PEMFCs.

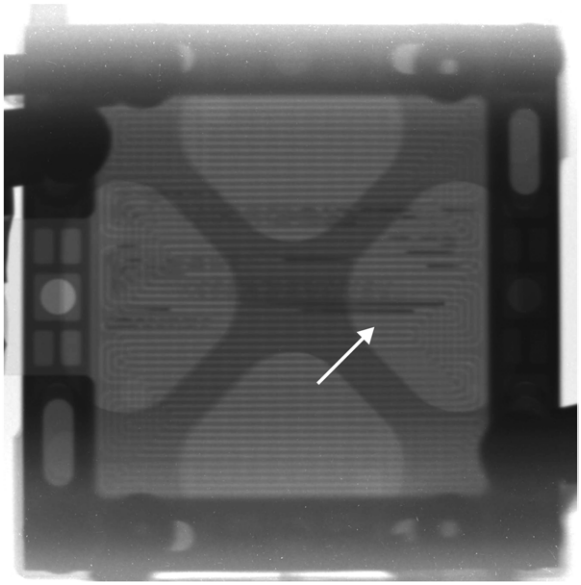

Figure 5. A radiographic image of an operating PEM fuel cell (size $140 \times 140\,\mathrm{mm}^2$). The dark horizontal lines indicate large water accumulations in the gas flow channels (arrow).

Recently, *in situ* investigations of liquid water agglomerations in PEMFCs have been reported using transparent fuel cells [56, 57], magnetic resonance imaging [58] and x-ray radiography [59–61]. However, neutron imaging is much better suited to observing and examining the water distribution and flow in an operating and unmodified fuel cell because neutrons are able to easily penetrate the metal housing of the cell, yet are extremely sensitive to even small amounts of water inside [42, 48, 62, 64–70]. Using neutron imaging, time resolutions of the order of several seconds are feasible, which is well matched with the typical time scale of these experiments. Figure 5 shows a normalized radiographic image of a single-stack fuel cell. The dark horizontal lines indicate water-flooded gas flow channels.

An example of the suitability of neutron radiography for quantitative analysis of the water content in gas diffusion layers (GDLs) of fuel cells is given in figure 6 [67]. GDLs are used for the transport of reactive gases to the catalysts on the anode and cathode side. They consist of carbon fibres and up to 20% polytetrafluoroethylene (PTFE) in order to increase the hydrophobicity. Figure 6 shows normalized neutron radiographs of three different types of GDL material with different PTFE contents. The water content was investigated at different current densities in an attempt to optimize the materials with respect to performance and cost.

Another example demonstrates the prospects of high-resolution detectors (in this case an MCP, see above), which allow very detailed imaging of the local water distribution on the anode and cathode side [31]. Figure 7 shows a cross-sectional (in-plane) view of an operating fuel cell at four different current densities. At $0.1\,\mathrm{A\,cm}^{-2}$ water can be found mostly on the cathode side and hardly any water is detected on

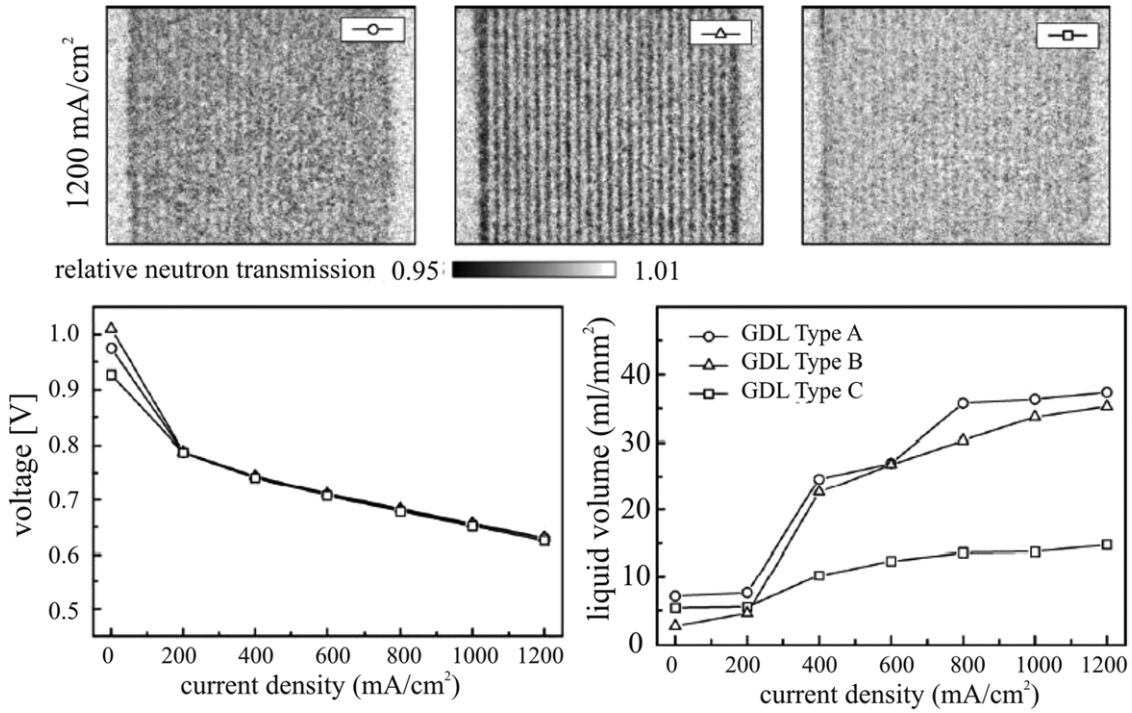

Figure 6. Three normalized neutron radiograms (top) showing the water content of three different GDL materials (from left to right: paper, paper, cloth, with a corresponding PTFE content of 5%, 17% and 0%, respectively). The water content within the GDL is dependent on the current densities of the fuel cell (bottom). (Reprinted with permission from [67]. Copyright 2006, Elsevier.)

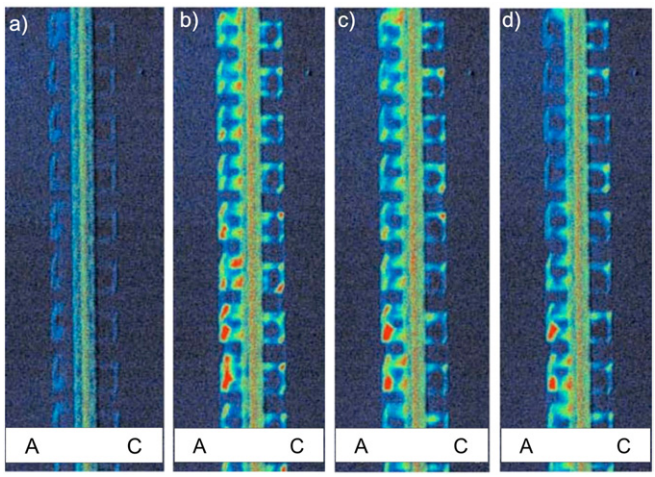

Figure 7. High-resolution neutron radiogram of an operating fuel cell at four different current densities: (*a*) 0 A cm^{-2}, (*b*) 0.1 A cm^{-2}, (*c*) 0.75 A cm^{-2} and (*d*) 1.25 A cm^{-2}. The images show the anode (A) and cathode (C) sides of the cell including the gas flow field channels and the MEA (membrane electrode assembly) consisting of GDLs, catalysts and a Nafion membrane [31].

the anode side. The distribution of small water droplets within the channels can be seen very clearly due to the high resolution of a few 10 μm. Above 0.75 A cm^{-2} a significant amount of water appears on the anode. Because of the increased water generation rate at increased current densities a large amount diffuses back to the anode side. However, at 1.25 A cm^{-2} the increasing heat in the cell allows faster evaporation of the water. Thus the overall water amount decreases again.

A recently developed approach is to use deuterium gas in place of normal hydrogen gas in order to exploit the contrast variation between the heavy water produced compared with the normal water present in the cell prior to the switch to using D_2. Thereby the liquid exchange characteristics of the cell could be studied and compared with the existing water transport models [63].

In addition to radiography, quasi-*in situ* tomographic investigations of multi-stack cells can be realized, enabling the distinction of several water-containing anodic and cathodic flow fields in three dimensions [48]. An example of this is shown in figure 8. The water distribution in the flow fields on both sides of the first cell within a triple PEM fuel cell stack has been quantified and is shown for two different current densities. At current densities around $I = 300$ mA cm^{-2} (figure 7(*a*)) similar amounts of liquid water are found on both sides, ensuring both a sufficient membrane humidification and a free gas flow. This is a result of the electro-osmotic drag being counterbalanced by back diffusion. In contrast, at $I = 500$ mA cm^{-2} the electro-osmotic drag increases, leading to a larger water accumulation on the cathode side and a corresponding and significant decrease in the water amount at the anode. The balance between electro-osmotic drag and back diffusion can also be changed by altering the properties of the materials used (e.g. membrane thickness).

4.2. Hydrogen storage

Mobile applications of fuel cells in vehicles or portable electronic devices require new materials that can store large amounts of hydrogen in high densities at low pressures and ambient temperatures with fast discharge/recharge characteristics. The hydrogen distribution inside a storage material, in particular under cyclic charge/recharging

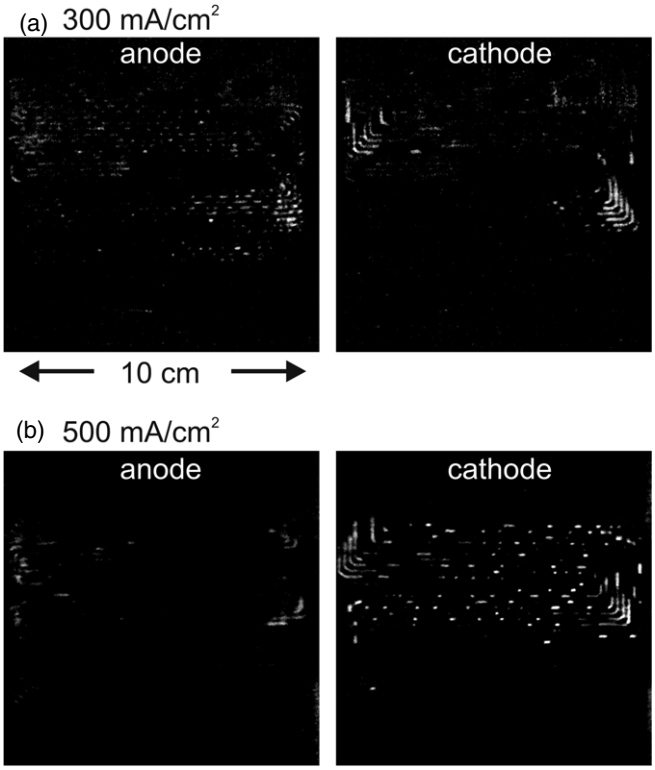

Figure 8. Water distributions in the anodic and cathodic flow-field channels of the first cell in a triple fuel cell stack at a current density of (*a*) $I = 300\,\mathrm{mA\,cm^{-2}}$ and (*b*) $I = 500\,\mathrm{mA\,cm^{-2}}$. (Reprinted with permission from [48]. Copyright 2007, American Institute of Physics.)

conditions, is therefore of great interest. Neutron radiographic [71] as well as tomographic [72] investigations have been conducted, e.g. on Mg–Ni alloys allowing hydrogen diffusion coefficients and volume expansion rates to be analysed. Figure 9 displays temporal changes in the hydrogen distribution in Mg–Ni alloy ingots hydrogenated in a $NaBH_4$ solution. The white parts relate to high attenuation coefficients caused by hydrogen absorption. After around 1 h the thickness of the hydrogen-containing area was around 1 mm.

4.3. Batteries

Internal structural changes during discharge influence the performance and lifetime of batteries. These structures are difficult to preserve when the metal housing has to be opened to analyse the interior, but they can be visualized using neutrons [36, 45]. Studies have been performed measuring a series of tomograms that map different stages of discharge. The example presented in figure 10(*a*) is a battery from a pacemaker for which the lifetime is particularly important. The battery is a lithium cell and, due to the lithium content, is highly attenuating (see figure 2). In this case, contrasting between the lithium interior and the metal casing was not an issue, but achieving sufficient beam transmission through the thickest dimension of the battery was critical. This study allowed the battery manufacturers to gain valuable information on the distribution of lithium, which was much less uniform than expected.

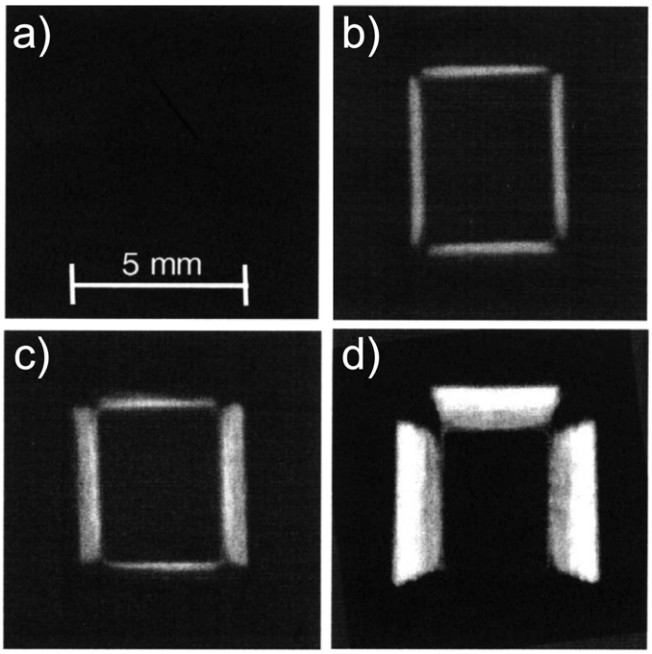

Figure 9. Neutron radiograms showing the hydrogen distribution in Mg–Ni alloy ingots after 0 (*a*), 0.25 (*b*), 0.5 (*c*) and 1 h (*d*) hydrogenation in a $NaBH_4$ solution. (Reprinted with permission from [71]. Copyright 2003, Elsevier.)

A further example is that of the distribution of intercalated hydrogen in an alkaline Zn–MnO_2 C-block battery (figure 10(*b*)). Figures 10(*c*) and (*d*) show cross-sections through the tomogram of the battery along the vertical and horizontal axes. In this case, changes in hydrogen density during discharge could be analysed. No significant variations in the attenuation density in the charged battery were found (figure 10(*c*)). However, the images do show some variations in the electrolyte content inside the separator fleece (see black arrows). After discharge, some hydrogen from the inner part (anode) was seen to have moved to the outer part (cathode), very close to the edge of the steel case. This results in a corresponding bright and dark ring in figure 10(*d*) (top) and bright and dark stripes in the corresponding image of figure 10(*d*) (bottom) (see red arrows). Such visualizations cannot be obtained by other techniques.

4.4. Engine components

Fuel and oil sediments in engine components such as those found in the tomographic reconstructions of combustion chambers shown in figure 11 could hinder the functioning of the entire engine and even lead to failure. In many cases such sedimentation is difficult to examine as it is located in inaccessible regions of massive metallic components and the sediments are too brittle and unstable to allow the relevant regions to be extracted, e.g. for microscopic investigations. Again, the ability of neutrons to penetrate metals and detect small amounts of hydrogen makes them ideal for such studies. The sediments can be identified and quantified in the reconstructed volume (figure 11, red arrows) and can then be evaluated by engineers with the aim of improving

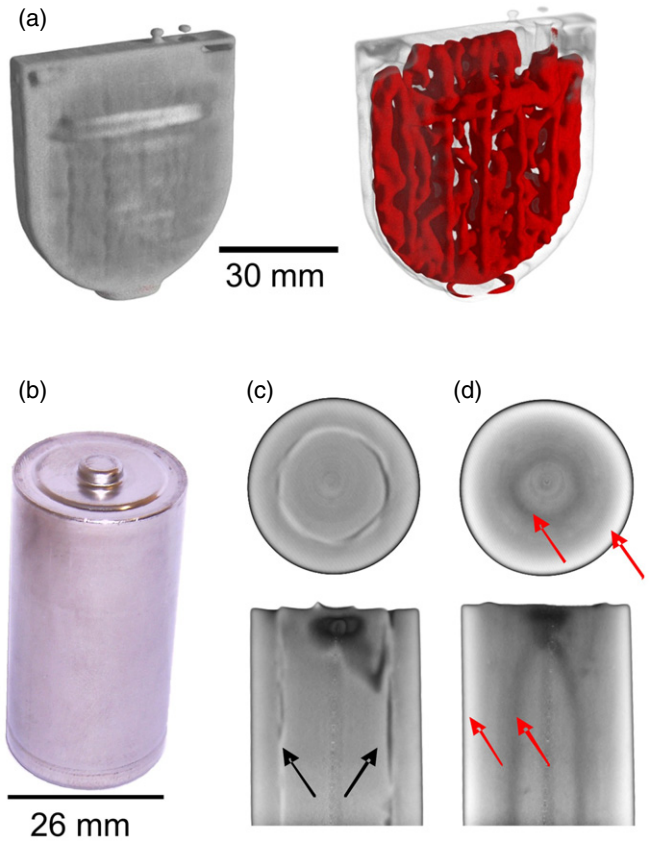

Figure 10. Top: tomographic reconstruction of a pacemaker battery showing the metal housing (left) and the lithium distribution within (right). Bottom: a neutron tomographic reconstruction of a C-block alkaline battery, showing a photograph (*b*) and cross-sections through the battery (*c*) before and (*d*) after discharge. The position of the electrolyte can be seen to shift (arrows in (*c*)) and some hydrogen shifts from the anode to the cathode (arrows in (*d*)).

the components such that sedimentation no longer occurs. Other applications of neutron imaging in this field include the analysis of soot contaminations in diesel particulate filters [36, 53, 73].

4.5. Running engines

When high flux densities are available, time-resolved studies of running processes are possible [36, 49, 50, 74–79]. One topic that has been addressed by time-resolved neutron radiography is the observation of running combustion engines with the aim of resolving and studying (for example) fuel injection or oil re-distribution. In order to achieve reasonable contrast and signal-to-noise ratios, i.e. to separate the injected fuel from the metal body of the engine, such measurements are carried out in a stroboscopic mode. The signal of the detector is synchronized with the cycle of the engine so that a number of images corresponding to the same position of the piston can be recorded during a series of strokes. The exposure time for each individual image is very short, but the accumulated series is equivalent to a much longer exposure time and the resulting image has better contrast and lower noise. This can be repeated for any piston position. In figure 12 parts of two separate measurement series performed at the ILL facility,

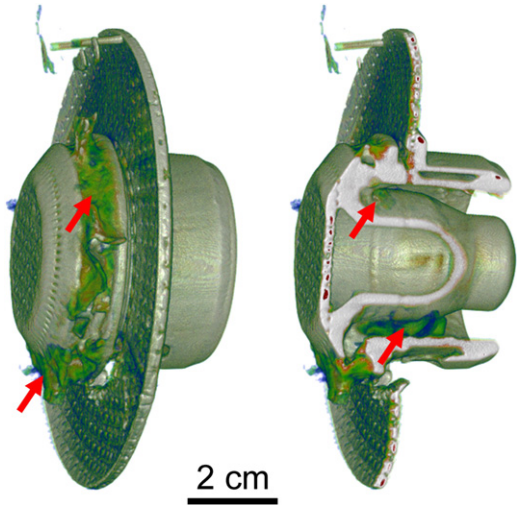

Figure 11. A tomographic reconstruction of a combustion chamber showing the metal casing and oil and fuel sediments (e.g. indicated by arrows).

Neutrograph [75], which provides the highest available neutron flux density (3×10^9 n cm^{-2} s^{-1}) are shown. In the upper part (figure 12(*a*)) two states of a motorbike engine running (driven by an electric motor) at 800 rpm are displayed. The images correspond to 250 μs time windows of the cyclic process, each being an accumulation of 60 images taken in phase with the motion. A number of such images taken consecutively over one period of the motion provides a time averaged movie of the process [34, 36, 74–79]. The images in figure 12(*b*) show fuel injection at 500 bar through a common rail diesel injection nozzle at 600, 700 and 800 μs. In this case 5000 images each of 100 μs exposure time taken at the same relative time of consecutive injections were accumulated for each represented image. Although the attenuation of the injected liquid is low (about 0.1%), it can be clearly visualized in the false-colour images [75]. Efforts to investigate larger engines and the corresponding fuel injection processes are still ongoing at high-flux radiography facilities, mainly at the FRM-II reactor in Munich [74, 79] and at the ILL in Grenoble [77, 78], where the limits of fast tomography are pushed to the maximum possible.

4.6. Plants

Another fascinating field of applications is the life sciences. As water plays a major role in all processes of life, a number of interesting questions can be addressed by neutron imaging in this field [80, 81]. The measurement presented in figure 13 was carried out in order to learn about water uptake of tomato plants [80]. The major challenge connected with this measurement was to visualize the water movements in the plant by using an image measured at time zero. As it is impossible to dehydrate the living organism before measurement, an approach that is commonly employed in neutron scattering was used; the plants were supplied with D_2O instead of H_2O—the differing neutron cross-sections of D and H were then exploited to yield contrast. This enabled the observation of the D_2O uptake when replacing H_2O in the plant. The plant was placed in the neutron beam and monitored before, during and after the D_2O–H_2O exchange

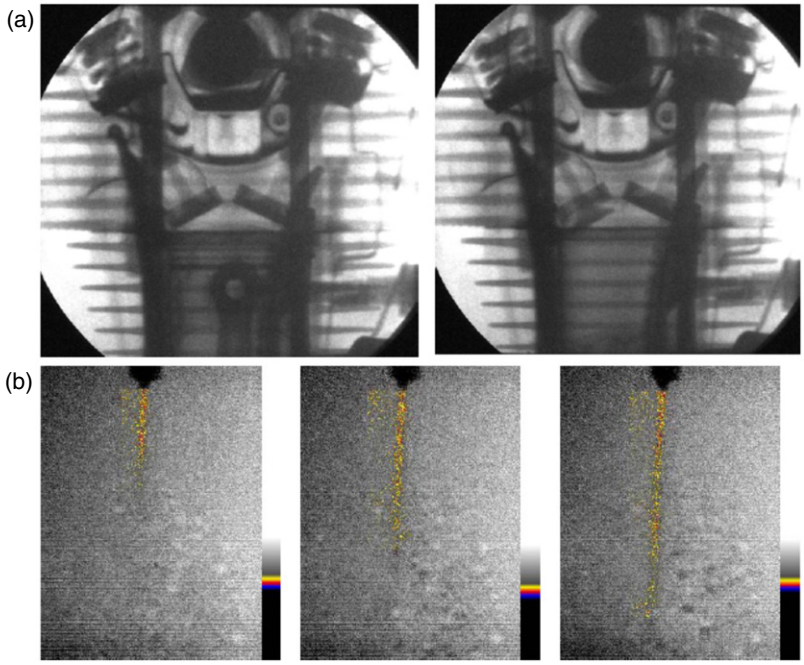

Figure 12. (*a*) Two images from a series of radiographs showing fast stroboscopic measurements of a running engine. Each image is an accumulation of 60 exposures of 250 μs each. The different positions of the piston and the ventiles are clearly visible. (*b*) Examples from a series of stroboscopic radiographies of a high pressure diesel injection nozzle. The time between the states shown is 100 μs and each image is an accumulation of 5000 exposures of 100 μs. (Reprinted with permission from [76]. Copyright 2005, IEEE.)

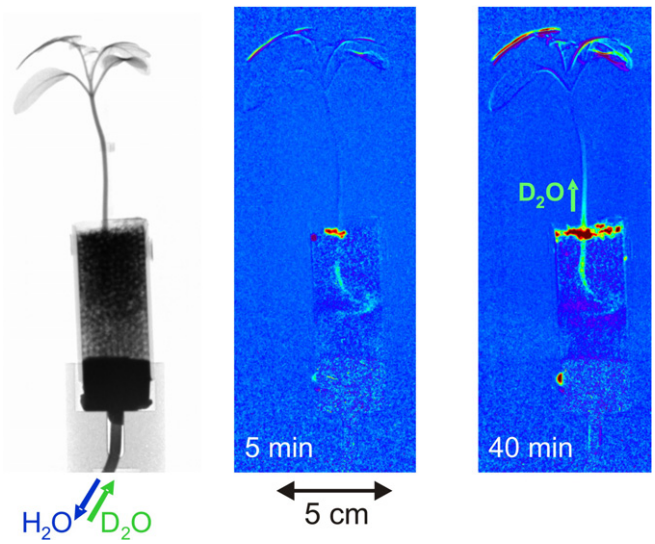

Figure 13. A radiograph of a tomato plant seedling before H_2O/D_2O exchange (left) and radiographs (normalized to the left-hand image) after H_2O/D_2O exchange. The changes in the roots/stem are caused by contrast between H_2O/D_2O (changes in the leaves are artefacts caused by movement during image acquisition).

in order to assess the stress induced both by the exchange and by the neutron irradiation. It was found that neither generates considerable stress and these results can therefore be considered as an investigation of the natural behaviour of the plant. An image was recorded prior to the exchange (i.e. with only H_2O in the plant) and all subsequent images were normalized to this image. Consequently, the normalized images only show the time-evolving changes in the H_2O–D_2O content of the plant. The displacement of H_2O by D_2O can be clearly seen in the roots and stem in figure 13 (centre and right). The leaves show artefacts due to plant movement during data acquisition—the contrast shown in these areas is not due to exchange processes.

4.7. Historical and archaeological objects

Valuable objects of historic or cultural interest have to be investigated non-destructively in order to preserve them [31, 82–84]. These objects are often combination of metals, stone and wood (coins, weapons and tools, for example), and may also be pieces of art. The example presented in figure 14(*a*) is a bronze statuette approximately 6.5 cm tall, most likely of Etruscan origin, dating from the third and fourth centuries BC [85]. Its interior was examined by neutron tomography to answer questions about the production techniques in use at that time. Several structural features inside the figure were identified with a spatial resolution of 200 μm and are most likely due to imperfections in the casting. Further conclusions have been drawn by specialists in this field [85]. Figure 14(*b*) displays a radiography of the lead filled bronze statuette 'Osiris from Thebe' dating from the eighth century BC. The image taken at the Ljubljana TRIGA Mark II research reactor (250 kW) illustrates that some valuable investigations with neutron imaging can even be done at small sources [86].

4.8. Rocks and stones

In geology, many questions are connected to the inner structure of rocks and stones, and are related to how stable a rock is, how it will break and how it developed. Depending on the stability of the pieces under investigation they can sometimes be sliced

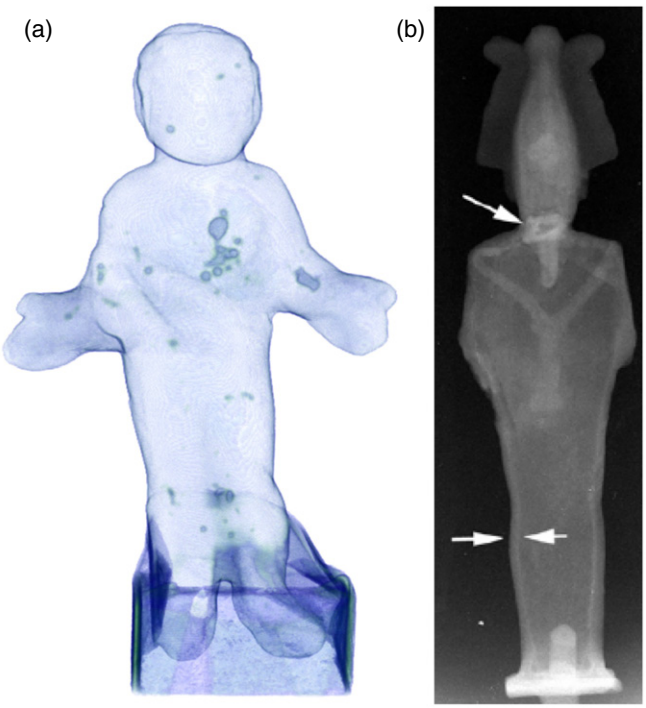

Figure 14. (*a*) A tomographic reconstruction of a Etruscan bronze statuette dating back to the third century BC. The dark features seen within the body are most likely defects produced during casting (height 65 mm). (*b*) The NR reveals the thickness of the bronze mantle, some cavities without lead and also a place where the head was fixed to the body by organic glue for restoration. (Reprinted with permission from [86].)

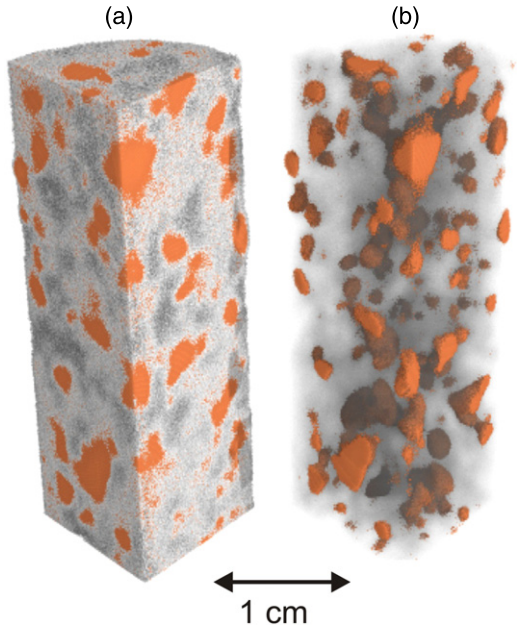

Figure 15. Tomographic reconstruction of a granite sample (*a*) showing the kaolinite highlighted (*b*).

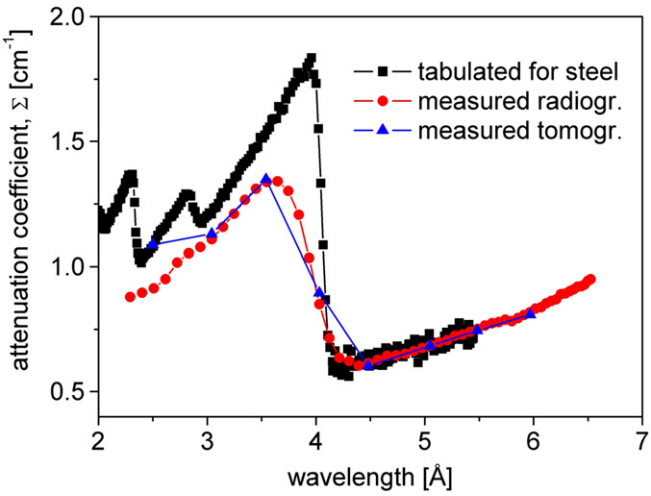

Figure 16. Tabulated and radiographically or tomographically [93] measured values of the neutron attenuation coefficient for iron.

to give an insight into their inner structure. However, neutron tomography—as in many cases also x-ray imaging—provides a fast and simple alternative that leaves the sample intact. Figure 15(*a*) shows an example of a granite sample studied to see the distribution of kaolinite ($Al_2Si_2O_5(OH)_4$) formed by the specific reaction of feldspar crystals ($KAlSi_3O_8$) with hot water. Consequently with neutrons a significant contrast can be achieved between the different constituents of the rock due to the involvement of hydrogen in the OH groups of the kaolinite. Aside from geologists, palaeontologists or (art) historians may be interested in the interior structure of stones and their inclusions (or other features) [77, 85].

5. New developments

Besides the many technical improvements and the ongoing optimization of 'standard' imaging setups and their components, some new methods have been developed recently that go beyond the established 3D mapping of neutron attenuation coefficients with polychromatic neutrons. The aim of these techniques is to increase the potential of neutron imaging, widen the range of possible application and introduce new ways of achieving image contrast in order to obtain additional structural information (e.g. nanostructure or magnetic field distribution). These methods along with their individual potential challenges and realizations will be described in the following section together with some possible applications.

5.1. Monochromatic-neutron imaging

Conventionally, the full energy spectrum available at a beam port is used for imaging as it affords the highest flux density. However, as stated above and as seen in figure 16, the attenuation coefficient can be strongly energy-dependent. Consequently, in conventional imaging a mean attenuation coefficient is measured,

$$\bar{\mu} = \frac{\int_{\Delta E} \mu(E) I(E) \mathrm{d}E}{\int_{\Delta E} I(E) \mathrm{d}E}, \tag{8}$$

depending on the spectrum $I(E)$ and the energy range ΔE used. For crystalline materials (e.g. most metals at room temperature) the increase in attenuation with neutron wavelength (i.e. with decreasing energy) caused by the nuclear cross-sections of a given material is superposed with a specific

crystal-lattice dependent pattern of what is referred to as Bragg edges. Bragg scattering removes neutrons from the transmitted beam. As the neutron wavelength λ is increased, the scattering angle 2Θ due to first-order Bragg reflection at a specific lattice plane d_{hkl} increases according to Bragg's law:

$$2d_{hkl} \sin \Theta = \lambda. \tag{9}$$

However, above the wavelength for which $\Theta = 90^\circ$ the Bragg condition can no longer be satisfied for the particular lattice plane. At this wavelength a Bragg edge is found in the attenuation spectrum and for longer wavelengths the attenuation coefficient drops significantly—this is illustrated in figure 16 for iron. Such edges are observed for many crystallographic planes, but the (1 1 0) discontinuity is the most significant in the bcc structure because it has the biggest lattice spacing (and hence is the last cut-off).

As a consequence, the beam spectrum (and with it the measured material attenuation coefficients) may change significantly along the path of the beam even through a homogeneous sample, since neutrons of certain wavelengths will be scattered or absorbed more than others and consequently (for different locations in the sample $(x, y) \neq (x', y')$)

$$\frac{I(x, y, E)}{\int_{\Delta E} I(x, y, E) \mathrm{d}E} \neq \frac{I(x', y', E)}{\int_{\Delta E} I(x', y', E) \mathrm{d}E}. \tag{10}$$

This in turn can cause strong artefacts in a tomographic reconstruction where a homogeneous material is not displayed as such. The utilization of monochromatic radiation avoids such disadvantages and enables much better quantification [87–89] and higher sensitivity at the price of significantly lower flux densities and longer exposure times.

Moreover, the specific absorption spectrum of a material can be exploited to enhance contrast. Methods have been developed using either a few distinct wavelengths or sequentially scanning a certain wavelength range (containing a Bragg edge) for imaging. These methods will be dealt with in later sections.

Several techniques can be used for monochromatization. A pulsed source (e.g. a spallation source) or choppers in a continuous beam can be used in combination with time-resolved data analysis. Neutrons of different wavelengths (i.e. different energies/velocities) will arrive at the detector at different times and this allows the energy dependence to be resolved [90].

Other options at continuous sources involve velocity selectors [91, 92] or crystal monochromators [87–89, 93, 94]. Several options have been realized at different facilities—each having advantages and disadvantages—and no qualitative comparison has been undertaken up to now; the optimum choice depends strongly on the envisaged application.

Time of flight (TOF) imaging requires a good time resolution of the imaging detector. This is a major challenge in itself and might compromise the spatial resolution, but it can deliver information for multiple wavelengths, which is useful when a wavelength band has to be scanned (cf section 5.3). Crystal monochromators and velocity selectors both select single wavelengths with the former generally giving better energy resolution than the latter, but the latter are simpler to implement. Crystal monochromators change the experimental geometry and this has to be considered carefully, in particular when they are implemented in an existing imaging setup. Combined approaches have also been reported [95].

In figure 17 a neutron tomogram of a vent pipe belonging to an aeroplane engine [36, 96] measured utilizing a beam monochromatized by a crystal monochromator is shown. Large and brittle sediments of fuel and oil were found inside the pipe. Neutron tomography was applied because other techniques would have destroyed the structure of the sediments, and x-rays failed to provide sufficient contrast. Monochromatic tomography was superior in this case because although conventional neutron tomograms could visualize the sediments, monochromatic neutrons provided the opportunity to distinguish between parts of the sediments with slightly different attenuation coefficients, as illustrated by the colour map. To distinguish between such areas was important in order to learn about the history and development of the sedimentation; sediments deposited earlier contain less hydrogen and therefore their attenuation is slightly lower than the ones deposited more recently. The use of monochromatic neutrons potentially improves and simplifies the quantification of tomographic results [88], which for polychromatic beams sometimes requires a great effort in treating data with correction algorithms [97–99].

5.2. Energy-selective imaging

For some problems it can be useful to carry out neutron imaging at more than one neutron energy since the attenuation behaviour of different materials can vary differently on neutron energy. This allows different materials or even different phases of the same material to be distinguished, and can also reveal the structure of a material that is masked by the presence of a highly attenuating component around it. Figure 18 shows a radiogram of a standard spark plug [91, 92]. If two energies E_1, E_2 are chosen for which the attenuation of steel has nearly the same value (one below and one above a Bragg edge of steel) such that $\mu_1(E_1) = \mu_1(E_2)$, but for which the electrode displays different attenuation cross-sections such that $\mu_2(E_1) \neq \mu_2(E_2)$, then the ratio of images recorded at these two wavelengths will render the steel transparent. Hence, the structure of the electrode inside the steel shielding becomes visible, as

$$\begin{aligned} I_1(E_1) &= I_0(E_1) \cdot \mathrm{e}^{-\mu_1(E_1)s_1} \mathrm{e}^{-\mu_2(E_1)s_2} \quad \text{and} \\ I_1(E_2) &= I_0(E_2) \cdot \mathrm{e}^{-\mu_1(E_2)s_1} \mathrm{e}^{-\mu_2(E_2)s_2} \\ &\approx I_0(E_2) \cdot \mathrm{e}^{-\mu_1(E_1)s_1} \mathrm{e}^{-\mu_2(E_2)s_2}, \quad \text{and therefore} \\ I_1(E_1)/I_1(E_2) &\approx I_0(E_1)/I_0(E_2) \cdot \mathrm{e}^{-\mu_2(E_1)s_2}/\mathrm{e}^{-\mu_2(E_2)s_2}. \end{aligned} \tag{11}$$

Only a dependence on μ_2 and the thickness s_2 of the material remains.

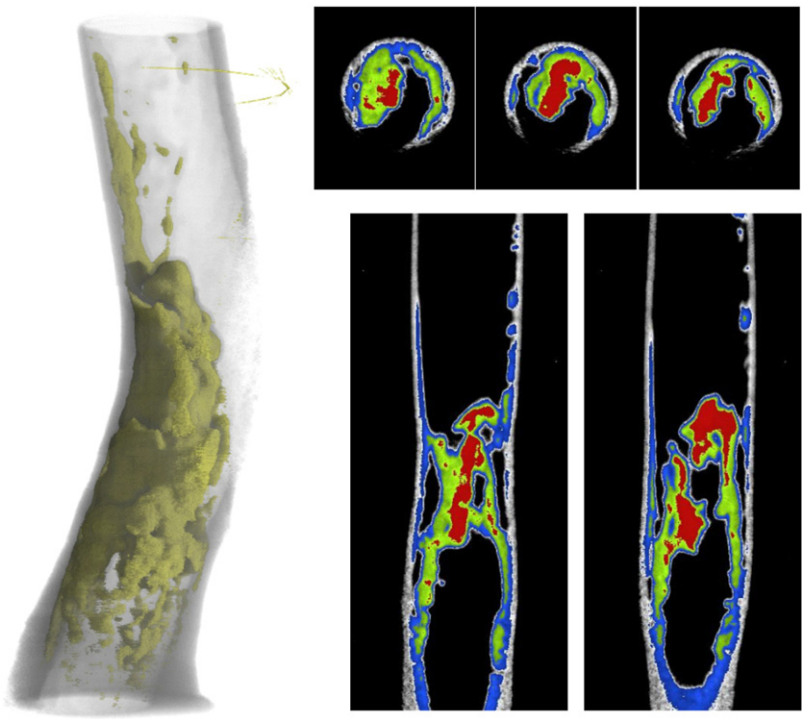

Figure 17. Tomographic reconstruction of an aircraft engine vent pipe measured with monochromatic neutrons showing oil and fuel sediments (2 cm diameter) [36]. The different colours/greyscales in the cross-sections through the pipe (right) indicate sediments of varying hydrogen content (red/darker grey means high hydrogen content).

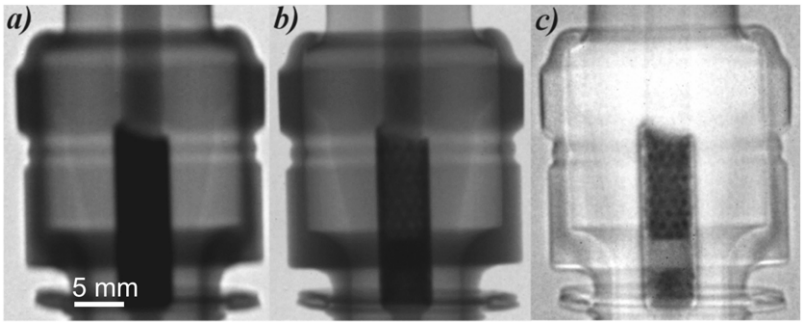

Figure 18. Radiographs of a spark plug measured with neutrons of wavelengths (*a*) 6.9 Å and (*b*) 3.2 Å [77, 84]. The electrode is masked by the steel in the initial images, but is revealed by taking (*c*) the ratio of the two images.

5.3. Energy-dispersive imaging

Enhanced imaging contrast can be produced by scanning through a wavelength range around a Bragg edge of a specific material because the attenuation spectra may differ for different regions of the same material $\mu(x, y, E) \neq \mu(x', y', E)$ due to differences in Bragg scattering related to the crystalline microstructure. Crystallographic phases and areas of different texture (e.g. caused by mechanical treatment) can be visualized in imaging experiments as the number of neutrons that they deflect at a defined wavelength differs slightly from that of the surrounding material (i.e. the Bragg-edge structure is different). This has been demonstrated in studies of texture-related structures in stir welds [90]. By recording images at many wavelengths around a specific Bragg edge the measured material attenuation coefficient for every pixel as a function of wavelength enables analysis of the Bragg edge, for every point of an image and to extract several relevant parameters—edge height, width and position. This information can be used to create new images that show how these parameters vary throughout the material [93]. This is demonstrated in figure 19, which shows a bent steel plate imaged at 43 different wavelengths in the range from 2.2 to 6.4 Å. The wavelength resolution $\Delta\lambda/\lambda$ was around 10% full width at half maximum. The image shows contrast in regions where the Bragg-edge position shifts, i.e. at the bent edges. In future these methods are expected to have the potential to support (or even partially replace) dedicated stress and strain diffraction measurements by identifying areas of interest with comparably little effort and a large field of view. However, it should be kept in mind that different applications require different wavelength resolutions. While it is possible to identify some texture alterations with wavelength resolutions of the order of 10^{-2}, dedicated stress investigation requires resolutions of the order of at least 10^{-3}. The new

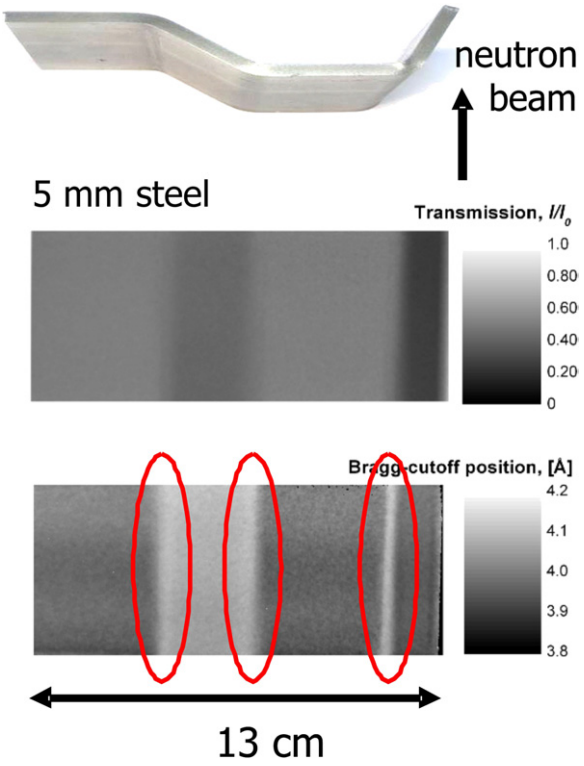

Figure 19. A photograph (top), radiograph (centre) and Bragg-edge position image (bottom) of a bent steel plate. The Bragg-edge image is calculated from the recorded attenuation spectra for every point in the image and displays significant contrast at the bends. (Reprinted with permission from [93]. Copyright 2006, American Institute of Physics.)

spallation sources available at present offer a great potential for this method because they can be utilized efficiently for spectroscopic measurements [100].

5.4. Phase-contrast imaging

Conventional neutron imaging is based purely on the attenuation of the beam by absorption and scattering. Besides attenuating a beam, a sample also interferes with the phase of the wave field and induces a phase shift $\Delta\varphi$. Absorption is related to the imaginary part of the refractive index, while the phase shift is connected to its real part, δ:

$$\delta \approx \frac{N b_c \lambda^2}{2\pi}, \tag{12}$$

which depends on the bound coherent scattering length b_c and the particle density N [87]. The phase shift $\Delta\varphi$ of the transmitted radiation can be expressed by

$$\Delta\varphi(\theta, t) = -k \int_{\text{path}} \delta(x, y)\mathrm{d}s, \qquad \text{with} \quad k = 2\pi/\lambda. \tag{13}$$

In cases where there is very little attenuation, detection of the phase shift can provide highly improved image contrast. However, the phase of radiation cannot be addressed as straightforwardly as the intensity. The only method to directly determine the phase for tomographic imaging is by (perfect crystal) interferometry [101, 102]. Differential neutron phase contrast methods [87, 88, 96, 103–107] measure the angular beam deviations $\Theta(\theta, t)$ induced by phase shifts $\Delta\varphi$:

$$\Theta(\theta, t) = \frac{1}{k}\nabla_\perp(\Delta\varphi(\theta, t)) = \frac{1}{k}\frac{\partial \int_{\text{ray}} \delta(x, y(x, \theta, t)) \cdot \mathrm{d}s}{\partial t}. \tag{14}$$

Such techniques enable the tomographic reconstruction of the real part of the refractive index distribution $\delta(x,y)$ via the path integral in equation (14) [87]. In conventional setups, intensity variations due to the angular deviations can be found by the propagation-based method if appropriate spatial resolution can be achieved [108–114]. All early approaches concerning these methods suffered from low flux densities caused either by collimation or by other beam preparation steps. In principle, tomography is possible [107], but is either very time consuming (exposure times of several days) or rather qualitative. Recently, another differential phase contrast technique developed for x-rays [115] has been realized with neutrons [116]. A grating-based shearing interferometer setup provides several advantages, namely relaxed collimation and energy resolution requirements, enabling higher flux densities and shorter exposure times. These experiments can be carried out at conventional imaging facilities and allow the refractive index distribution to be reconstructed quantitatively, something that was previously achievable only using perfect crystal optics [117].

5.5. Dark-field (USANS) contrast

Double-crystal setups used for differential phase contrast imaging can additionally provide image data based on (ultra) small-angle scattering even for tomography [106] (see figures 20(*b*) and (*c*)). Ultra small-angle scattering provides information about the microstructure in a sample, i.e. on a length scale complementing the resolvable range of real space methods [89]. This kind of contrast mechanism is called dark-field or extinction contrast due to analogies to comparable x-ray methods [118]. The scattering-induced width B of the angular distribution of a ray can be measured and approximated by the path integral

$$B(\theta, t) = \sqrt{\int_{\text{path}} \frac{\sigma(x, y) N(x, y)}{R^2(x, y)} \mathrm{d}s}, \tag{15}$$

which in turn enables conventional tomographic reconstruction of the scattering parameter described by the correlation length R and the reciprocal mean free path length σN, with σ being the scattering cross-section and N the particle density. However, the flux densities in a neutron double-crystal diffractometer are too low for most practical applications. It has been demonstrated only recently that a USANS, i.e. a dark-field, signal (adding to the point spread function) can also be extracted from the data acquired by the grating interferometer method used for differential phase contrast imaging [119]. Consequently, dark-field contrast imaging has gained the potential to become a powerful tool to investigate inhomogeneities on a micro- to mesoscopic scale of structures within a sample, and hence to add valuable three-dimensional information. Additionally, as for double crystal diffractometer

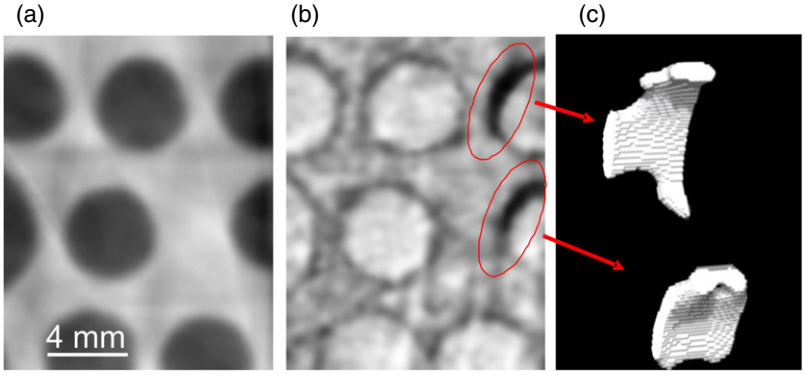

Figure 20. A tomographic reconstruction of a piece of aluminium containing several drilled holes (4 mm diameter) showing (*a*) the refractive index distribution (from differential phase contrast data), (*b*) dark-field contrast (displaying additional image contrast due to sediments) and (*c*) a three-dimensional rendering of a sediment found in the dark-field tomogram. (Reprinted with permission from [119]. Copyright 2008, American Physical Society.)

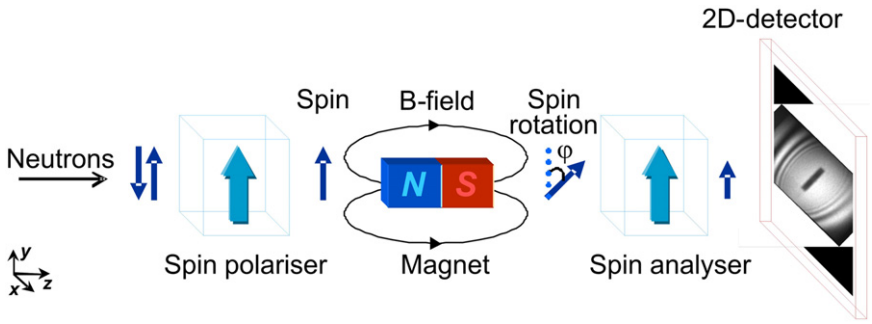

Figure 21. Setup used for polarized-neutron imaging [125].

attenuation contrast, differential phase contrast and dark-field contrast are measured simultaneously during a tomographic measurement. The measurements of a single projection image revealing these parameters are based on scans comprising multiple steps (typically up to 10 images are recorded) in order to achieve angular information.

5.6. *Polarized neutron imaging*

Another useful feature of neutrons is the magnetic moment (and spin) they carry, making them sensitive to magnetic fields. Ideas for utilizing this for imaging magnetic fields have been proposed for at least a decade [120–124]. However, only recently have efforts been made at different imaging facilities to take advantage of the unique possibility to image magnetic fields not only in free space but also within bulk material.

The magnetic moment of the neutron, $\vec{\mu}$ (-9.66×10^{-27} J T^{-1}) is aligned anti-parallel to its associated spin. An externally applied magnetic field $\vec{B}$ causes a precession of the spin vector around the field vector by an angle

$$\varphi_s = \frac{\gamma}{v} \int B \, \mathrm{d}s = \frac{\gamma \lambda m}{2\pi\hbar} \int B \, \mathrm{d}s, \tag{16}$$

where m is the mass of the neutron (1.675×10^{-27} kg), γ is the gyromagnetic ratio of the neutron (-1.8324×10^8 rad s^{-1} T^{-1}) and $B = |\vec{B}|$.

A combination of polarization analysis with standard radiographic and tomographic imaging allows the visualization of magnetic field distributions in real space. The principle of polarized neutron imaging is described in figure 21. A neutron beam is polarized, after which the neutrons traverse the magnetic field in free space or inside the sample. The final precession angle of the neutron spin is measured with spatial resolution using a spin analyser in front of the imaging detector. For monochromatic neutrons with a uniform velocity, the precession angle can be related to the field integral along the path of the neutrons through the field, see equation (16).

The resulting two-dimensional projection image is a product of the contrast given by the spin analysis due to the spin rotation, $I_m(x, y)$, and the conventional attenuation image, $I_a(x, y)$:

$$I(x, y) = I_0(x, y) \cdot \underbrace{\exp\left(-\int_{\text{path}} \Sigma(s)\mathrm{d}s\right)}_{I_a(x,y)/I_0(x,y)} \times \underbrace{\frac{1}{2}(1 + \cos\varphi_s(x, y))}_{I_m(x,y)/I_0(x,y)}. \tag{17}$$

Magnetic fields within samples, which are not amenable to any other available measurement technique, can be investigated and visualized even three dimensionally, opening a whole new field of applications investigating magnetic fields and electric currents in the bulk of massive samples. First promising results have been reported by different groups [125–130].

Figure 22(*a*) shows a radiogram of a permanent dipole magnet levitating over a superconducting YBCO sample. The

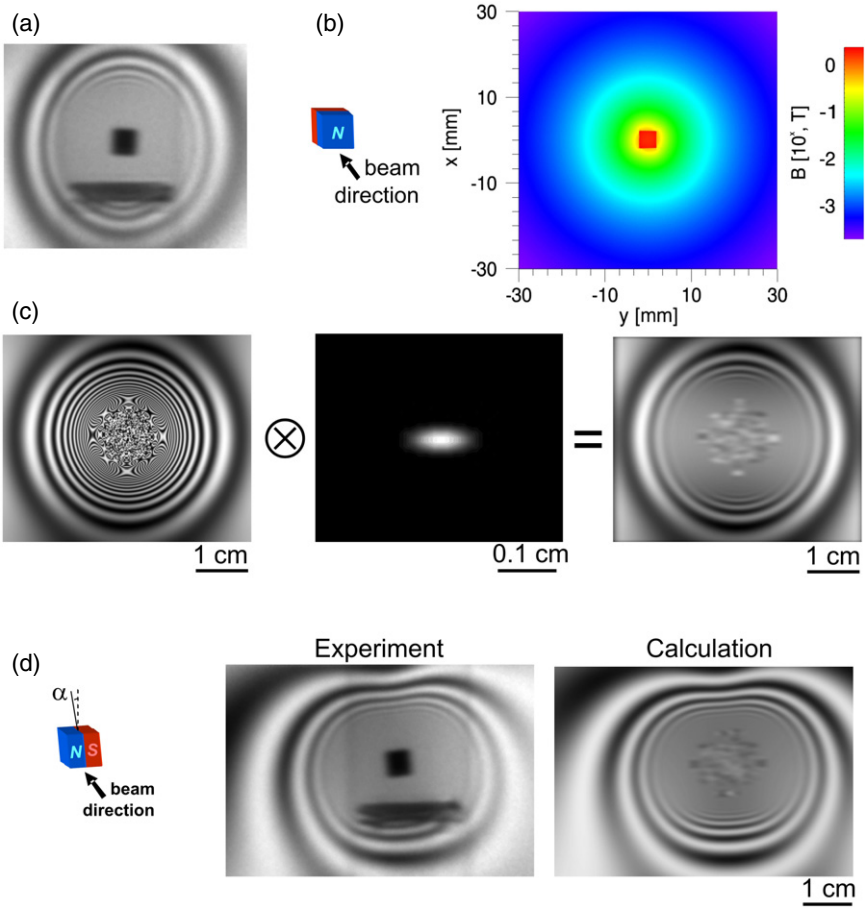

Figure 22. A comparison of measured and simulated radiographs of the magnetic field distribution around a permanent magnet showing (*a*) the dipole magnet levitating over an YBCO superconductor; (*b*) a diagram of the dipole orientation and the calculated magnetic field distribution in the plane perpendicular to the dipole axis; (*c*) the calculated radiograph (for polarized neutrons) and blurring due to limited spatial resolution (the artefacts in the central region are caused by the limited sampling and the strong magnetic field close to the magnet); (*d*) a measured and simulated radiograph for a tilted dipole ($\alpha = 4^\circ$) [125].

radial decrease in the relatively strong magnetic field gives rise to an annular structure due to the cosine function of the magnetic contrast (equation (17)). In the central region of the image this structure vanishes owing to the limited spatial resolution and the decreasing radial period caused by the field. Excellent agreement with theoretical predictions, in particular when taking into account the true spatial resolution, has been found.

In a first step, the dipole field of the magnet was calculated using Biot–Savart's law. Figure 22(*b*) displays the distribution of the magnetic field strength in a plane perpendicular to the dipole axis (through the centre of the magnet). The calculated field distribution was then used to determine the expected spin rotation along the flight path of the neutrons using equation (16), yielding the expected radiogram (figure 22(*c*)). The resulting radiogram has been convoluted with a Gaussian resolution function to simulate the finite resolution of the setup. When the permanent magnet is tilted, the annular structure is altered correspondingly (figure 22(*d*)). A fitting procedure was applied and the orientation of the dipole could be determined by the best fit between the calculated and the measured image. An example of a first demonstrative application to an effect related to superconductivity, namely the Meissner effect, is presented in figure 23, showing a superconductive YBCO sample above and below its critical temperature of 90 K. The displacement of the magnetic field due to the Meissner effect is clearly visible (figure 23(*c*)).

5.7. Phase contrast and polarized neutrons

Neutron phase contrast imaging methods are also suitable for exploring magnetic fields and structures due to a magnetic-field-induced contribution to the real part of the refractive index (and hence to the phase distribution of penetrating neutron radiation). Such methods were introduced several decades ago, but their potential has only been realized recently with the advent of efficient phase contrast methods (see above). Magnetic fields add to the real part of the refractive index the spin-dependent term

$$\delta_\mu \sim \pm \mu B m \lambda^2 / h^2. \tag{18}$$

Consequently, magnetic fields can be measured by phase-contrast methods. This was demonstrated with radiographic images of the magnetic domains in a ferromagnetic sample recorded using polarized neutrons in a perfect crystal interferometer in the early 1980s [131]. A pair of

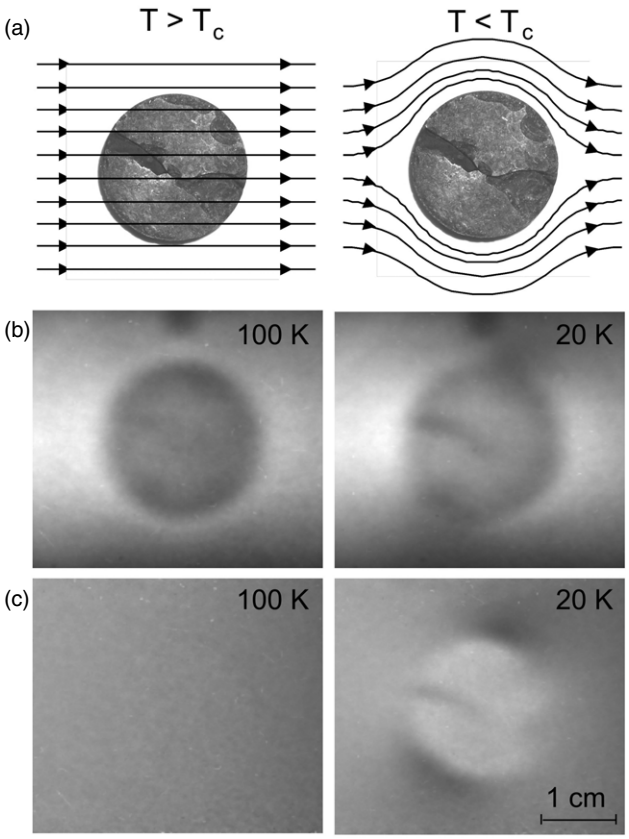

Figure 23. (*a*) A schematic diagram of the expulsion of magnetic field lines by a superconductor below the critical temperature T_c—the so-called Meissner effect. (*b*) Radiographs of a superconducting YBCO pellet in a magnetic field above (left) and below (right) the critical temperature ($T_c = 90$ K) measured with polarized neutrons. (*c*) The radiographs shown in (*b*) are normalized to a reference image taken in zero field at 100 K (i.e. a pure attenuation image) such that only magnetic contrast is exhibited [125].

corresponding measurements with spin-up and spin-down neutrons enables quantitative measurements and makes it possible to distinguish between nuclear and magnetic-field-induced phase shifts. This can be demonstrated using a double-crystal diffractometer for polarized differential phase-contrast tomography [132]. Indeed, phase-contrast images of magnetic structures can be achieved even with non-polarized beams. The spin states split due to the opposite phase shifts for spin-up and spin-down neutrons. As long as the angular splitting measured in a differential phase contrast setup is moderate, a dark-field contrast-like signal [133] provides images of magnetic field distributions, as reported in 1994 in the course of presenting radiographs recorded in a double-crystal setup [134]. Recently, similar results achieved with the now available shearing interferometer technique have been reported [135]. A corresponding image of the vertical domain structure in terms of the corresponding Bloch walls of a ferromagnetic plate is shown in figure 24.

6. Summary

Neutron radiography and tomography are still developing, including technical improvements and the optimization of a

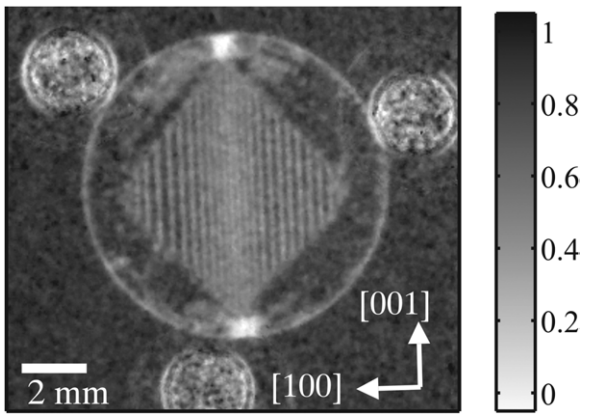

Figure 24. A dark-field contrast image of the magnetic domain structure in a ferromagnetic FeSi single crystal disc. (Reprinted with permission from [135]. Copyright 2008, American Institute of Physics.)

growing number of dedicated instruments at the world's major neutron sources, as well as the introduction and establishment of new neutron imaging concepts. Triggered by the recent progress that is reflected by both instrumental and methodical achievements, the field of applications is growing both in number and in scope, and the outstanding abilities of neutron imaging for the exploration of materials and components are now being realized. Scientific applications range from archaeology, art, history, life sciences and biology to materials science and physics, much of which is beyond the scope of this paper. Nevertheless, some demonstrative examples have been introduced in order to underline the outstanding potential of neutron imaging. Furthermore, the importance of neutron imaging for non-destructive investigations of valuable and fragile objects has been outlined. The field of applications is still growing and the quality and the potential of the various techniques are constantly improving. Neutron imaging techniques are now able to address microstructural variations of samples relevant to materials science and engineering, and can also visualize and investigate non-material quantities such as magnetic fields and electric currents in bulk solid samples.

Acknowledgments

The authors would like to thank Christoph Hartnig for providing ideas for configuration of the section 'Fuel cells'. The research activities were partly funded by the German Federal Ministry for Education and Science (BMBF) under grant numbers 03SF0324A and 03SF0324F.

References

[1] Kuhn E *US Patent* No 2186 757. http//www.uspto.gov/patft/
[2] Berger H, Talboy J H and Tylka J P 1964 Determination of cadmium burnup in reactor control rods by neutron radiography *Nucl. Sci. Eng.* **18** 236
[3] Maier-Leibnitz H and Springer T 1963 The use of neutron optical devices on beam-hole experiments *Nucl. Sci. Technol.* **17** 217
[4] Schillinger B 1999 Neue Entwicklungen zu Radiographie und Tomographie mit thermischen Neutronen und zu deren routinemäßigen Einsatz *PhD Thesis* TU München

[5] Körner S 2000 Digital image processing in neutron radiography *PhD Thesis* TU Wien

[6] Lehmann E H 2000 Facilities for neutron radiography in Europe: performance, applications and future use *Proc.15th World Conf. on Non-destructive Testing (Rome, Italy, October 2000)* (Brescia, Italy: AIPnD)

[7] de Broglie L 1923 Waves and quanta *Nature* **112** 540

[8] Bücherl T, Kutlar E, Lierse von Gostomski C, Calzada E, Pfister G and Koch D 2004 Radiography and tomography with fast neutrons at the FRM-II—a status report *Appl. Radiat. Isot.* **61** 537

[9] Hausladen P A, Bingham P R, Neal J S, Mullens J A and Mihalczo J T 2007 Portable fast-neutron radiography with the nuclear materials identification system for fissile material transfers *Nucl. Instrum. Methods* B **261** 387

[10] Banhart J (ed) 2008 *Advanced Tomographic Methods in Materials Research and Engineering* (Oxford: Oxford University Press)

[11] Radon J 1917 *Ber. Sächsischer Akad. Wiss.* **29** 262

[12] Gaskill J D 1978 *Linear Systems, Fourier Transforms and Optics* (New York: Wiley)

[13] Kak A C and Slanley M 1988 *Principles of Computerised Tomographic Imaging* (New York: IEEE Press)

[14] Rehacek J, Hradil Z, Zawisky M, Treimer W and Strobl M 2002 Maximum-likelihood absorption tomography *Europhys. Lett.* **59** 694

[15] Kuba A, Rodek L, Kiss Z, Rusko L, Nagy A and Balasko M 2005 Discrete tomography in neutron radiography *Nucl. Instrum. Methods* A **542** 376

[16] Krimmel S, Baumann J, Kiss Z, Kuba A, Nagy A and Stephan J 2005 Discrete tomography for reconstruction from limited view angles in non-destructive testing *Electron. Notes Discrete Math.* **20** 455

[17] Ali A M, Melegy Z, Morsy M, Megahid R M, Bucherl T and Lehmann E H 2004 Image reconstruction techniques using projection data from transmission method *Ann. Nucl. Energy* **31** 1415

[18] de Beer A *et al* 2000 *Nucl. Instrum. Methods* B **170** 259
Reijonen J 2007 *Nucl. Instrum. Methods* B **261** 272
Bücherl T *et al* 2004 *Appl. Radiat. Isot.* **61** 659

[19] Schillinger B, Bleuel M, Boni P, Steichele E 2005 Design and simulation of neutron optical devices plus flight tube for neutron radiography *Proc. 7th World Conf. on Neutron Radiography (WCNR-7, Rome, Italy, 2005)* ed P Chirco and R Rosa (Rome: ENEA)

[20] Kardjilov N, Böni P, Hilger A, Strobl M and Treimer W 2005 Characterization of a focusing parabolic guide using neutron radiography method *Nucl. Instrum. Methods* A **542** 248

[21] Kardjilov N, Hilger A, Manke I, Strobl M, Treimer W and Banhart J 2008 Multifunctional tomography instrument with cold neutrons at HMI *Proc. 8th World Conf. on Neutron Radiography (WCNR-8, Gaithersburg, USA, 2006)* ed M Arif and R G Downing (Lancaster, PA: DESTech Publ. Inc.)

[22] Granfors P R and Aufrichtig R 2000 Performance of a 41×41-cm^2 amorphous silicon flat panel x-ray detector for radiographic imaging applications *Med. Phys.* **27** 6

[23] Siewerdsen J H, Antonuk L E, El-Mohri Y, Yorkston J and Huang W 1998 Signal, noise power spectrum, and detective quantum efficiency of indirect-detection flat-panel imagers for diagnostic radiology *Med. Phys.* **25** 5

[24] Lehmann E and Vontobel P 2004 The use of amorphous silicon flat panels as detector in neutron imaging *Appl. Radiat. Isot.* **61** 567

[25] Estermann M, Lehmann E, Frei G and Vontobel P 2005 The performance of an amorphous silicon flat panel for neutron imaging at the PSI NEUTRA facility *Nucl. Instrum. Methods* A **542** 253

[26] Pleinert H, Lehmann E and Körner S 1997 Design of a new CCD-camera neutron radiography detector *Nucl. Instrum Methods* A **399** 382

[27] Frei G, Lehmann E H, Zeller R and Walfort B 2008 Optimization of neutron sensitive imaging scintillators *Proc. 8th World Conf. on Neutron Radiography (WCNR-8, Gaithersburg, USA, 2006)* ed M Arif and R G Downing (Lancaster, PA: DESTech Publ. Inc.)

[28] Lehmann E H, Frei G, Kühne G and Boillat P 2007 The micro-setup for neutron imaging: A major step forward to improve the spatial resolution *Nucl. Instrum. Methods* A **576** 389

[29] 2007 own unpublished results

[30] Siegmund O H, Vallerga J V, Tremsin A S, Mcphate J and Feller B 2007 High spatial resolution neutron sensing microchannel plate detectors *Nucl. Instrum. Methods* A **576** 178

[31] Hickner M A, Siegel N P, Chen K S, Hussey D S, Jacobson D L and Arif M 2008 Understanding liquid water distribution and removal phenomena in an operating PEMFC via neutron radiography *J. Electrochem. Soc.* **155** B427

[32] Boillat P, Scherer G G, Wokaun A, Frei G and Lehmann E H 2008 Transient observation of ^{2}H labeled species in an operating PEFC using neutron radiography *Electrochem. Commun.* **10** 1311

[33] Fiori F, Giunta G, Hilger A, Kardjilov N and Rustichelli F 2006 Non-destructive characterization of archaeological glasses by neutron tomography *Physica* B **385–386** 1206

[34] Hilger A, Kardjilov N, Strobl M, Treimer W and Banhart J 2006 The new cold neutron radiography and tomography instrument CONRAD at HMI Berlin *Physica* B **385–386** 1213

[35] Bastürk M, Arztmann J, Jerlich W, Kardjilov N, Lehmann E and Zawisky M 2005 Analysis of neutron attenuation in boron-alloyed stainless steel with neutron radiography and JEN-3 gauge *J. Nucl. Mater.* **341** 189

[36] Kardjilov N, Hilger A, Manke I, Strobl M, Treimer W and Banhart J 2005 Industrial applications at the new cold neutron radiography and tomography facility of the HMI *Nucl. Instrum. Methods* A **542** 16

[37] Bastürk M, Kardjilov N, Rauch H and Vontobel P 2005 Neutron imaging of fiber-reinforced materials *Nucl. Instrum. Methods* A **542** 106

[38] Lehmann E H, Vontobel P and Kardjilov N 2004 Hydrogen distribution measurements by neutrons *Appl. Radiat. Isot.* **61** 503

[39] Kaestner A, Hassanein R, Vontobel P, Lehmann P, Schaap J, Lehmann E and Flühler H 2007 Mapping the 3D water dynamics in heterogeneous sands using thermal neutrons *Chem. Eng. J.* **130** 79

[40] Grosse M. Lehmann E, Vontobel P and Steinbrueck M 2006 Quantitative determination of absorbed hydrogen in oxidised zircaloy by means of neutron radiography *Nucl. Instrum. Methods* A **566** 739

[41] Michaloudaki M, Lehmann E and Kosteas D 2005 Neutron imaging as a tool for the non-destructive evaluation of adhesive joints in aluminium *Int. J. Adhesion Adhesives* **25** 257

[42] Kramer D, Lehmann E, Frei G, Vontobel P, Wokaun A and Scherer G G 2005 An on-line study of fuel cell behavior by thermal neutrons *Nucl. Instrum. Methods* A **542** 52

[43] Lehmann E, Hartmann S and Wyer P 2005 Neutron radiography as visualization and quantification method for conservation measures of wood firmness enhancement *Nucl. Instrum. Methods* A **542** 87

[44] Lehmann E, Vontobel P and Estermann M 2004 Study of material changes of SINQ target rods after long-term

exposure by neutron radiography methods *Appl. Radiat. Isot.* **61** 603

[45] Goers D, Holzapfel M, Scheifele M, Lehmann E, Vontobel P and Novák P 2004 *In situ* neutron radiography of lithium-ion batteries: the gas evolution on graphite electrodes during the charging *J. Power Sources* **130** 221

[46] http://neutra.web.psi.ch/publication/Neutron_Imaging_e_Nutzer.pdf

[47] Lehmann E H, Vontobel P and Hermann A 2003 Non-destructive analysis of nuclear fuel by means of thermal and cold neutrons *Nucl. Instrum. Methods* A **515** 745

[48] Manke I, Hartnig C H, Grünerbel M, Kaczerowski J, Lehnert W, Kardjilov N, Hilger A, Treimer W, Strobl M and Banhart J 2007 Quasi-*in situ* neutron tomography on polymer electrolyte membrane fuel cell stacks *Appl. Phys. Lett.* **90** 184101

[49] Balaskó M, Jancsó G and Korösi F 2004 Analyzing of segregation in mixtures of 3-methylpyridine and heavy water by dynamic neutron radiograph *Appl. Radiat. Isot.* **61** 597

[50] Saito Y, Mishima K and Matsubayashi M 2004 Void fraction and velocity measurement of simulated bubble in a rotating disc using high frame rate neutron radiography *Appl. Radiat. Isot.* **61** 667

[51] Richards W J, Barrett J R, Springgate M E and Shields K C 2004 Neutron radiography inspection of investment castings *Appl. Radiat. Isot.* **61** 675

[52] Cimbala J M, Brenizer J S, Chuang A P-Y, Hanna S, Conroy C T, El-Ganayni A A and Riley D R 2004 Study of a loop heat pipe using neutron radiography *Appl. Radiat. Isot.* **61** 701

[53] Ismail B, Ewing D, Chang J-S and Cotton J S 2004 Development of a non-destructive neutron radiography technique to measure the three-dimensional soot deposition profiles in diesel engine exhaust systems *J. Aerosol Sci.* **35** 1275

[54] Vielstich W, Lamm A and Gasteiger H A (ed) 2003 *Handbook of Fuel Cells: Fundamentals, Technology and Applications* vol 3 (Chichester: Wiley)

[55] Carette L, Steele K A and Stimming U 2001 Fuel cells fundamentals and applications *Fuel Cells* **1** 5

[56] Yang X G, Zhang F Y, Lubawy A L and Wang C Y 2004 Visualisation of liquid water transport in a PEFC *Electrochem. Solid-State Lett.* **7** 408

[57] Tüber K, Pócza D and Hebling C 2003 Visualisation of water buildup in the cathode of a transparent PEM fuel cell *J. Power Sources* **124** 403

[58] Feindel K W, Bergens S H and Wasylishen R E 2006 Insights into the distribution of water in a self-humidifying H_2/O_2 proton-exchange membrane fuel cell using 1H NMR microscopy *J. Am. Chem. Soc.* **128** 14192

[59] Manke I, Hartnig Ch, Grünerbel M, Lehnert W, Kardjilov N, Haibel A, Hilger A, Riesemeier H and Banhart J 2007 Investigation of water evolution and transport in fuel cells with high resolution synchrotron x-ray radiography *Appl. Phys. Lett.* **90** 174105

[60] Hartnig Ch, Manke I, Kuhn R, Kardjilov N, Banhart J and Lehnert W 2008 Cross-sectional insight in the water evolution and transport in polymer electrolyte fuel cells *Appl. Phys. Lett.* **90** 134106

[61] Sinha P K, Mukherjee P P and Wang C Y 2007 Impact of GDL structure and wettability on water management in polymer electrolyte fuel cells *J. Mater. Chem.* **17** 3089

[62] Hartnig Ch, Manke I, Kardjilov N, Hilger A, Grünerbel M, Kaczerowski J, Banhart J and Lehnert W 2008 Combined neutron radiography and locally resolved current density measurements of operating PEM fuel cells *J. Power Sources* **176** 452

[63] Manke I, Hartnig Ch, Kardjilov N, Messerschmidt M, Hilger A, Strobl M, Lehnert W and Banhart J 2008 Characterization of water exchange and two-phase flow in porous gas diffusion materials by hydrogen–deuterium contrast neutron radiography *Appl. Phys. Lett.* **92** 244101

[64] Chen Y-S, Peng H, Hussey D S, Jacobson D L, Tran D T, Abdel-Baset T and Biernacki M 2007 Water distribution measurement for a PEMFC through neutron radiography *J. Power Sources* **170** 376

[65] Trabold T A, Owejan J P, Jacobson D L, Arif M and Huffman P R 2006 *In situ* investigation of water transport in an operating PEM fuel cell using neutron radiography: 1. Experimental method and serpentine flow field results *Int. J. Heat Mass Transfer* **49** 4712

[66] Owejan J P, Trabold T A, Jacobson D L, Baker D R, Hussey D S and Arif M 2006 *In situ* investigation of water transport in an operating PEM fuel cell using neutron radiography: 2. Transient water accumulation in an interdigitated cathode flow field *Int. J. Heat Mass Transfer* **49** 4721

[67] Zhang J, Kramer D, Shimoi R, Ono Y, Lehmann E, Wokaun A, Shinohara K and Scherer G G 2006 *In situ* diagnostic of two-phase flow phenomena in polymer electrolyte fuel cells by neutron imaging: B. Material variations *Electrochim. Acta* **51** 2715

[68] Pekula N, Heller K, Chuang P A, Turhan A, Mench M M, Brenizer J S and Ünlü K 2005 Study of water distribution and transport in a polymer electrolyte fuel cell using neutron imaging *Nucl. Instrum. Methods Phys. Res.* A **542** 134

[69] Satija R, Jacobson D L, Arif M and Werner S A 2004 *In situ* neutron imaging technique for evaluation of water management systems in operating PEM fuel cells *J. Power Sources* **129** 238

[70] Boillat P, Kramer D, Seyfang B C, Frei G, Lehmann E, Scherer G G, Wokaun A, Ichikawa Y, Tasaki Y and Shinohara K 2008 *In situ* observation of the water distribution across a PEFC using high resolution neutron radiography *Electrochem. Commun.* **10** 546

[71] Sakaguchi H, Satake Y, Hatakeyama K, Fujine S, Yoneda K, Matsubayashic M and Esaka T 2003 Analysis of hydrogen distribution in hydrogen storage alloy using neutron radiography *J. Alloys Compounds* **354** 208

[72] Sakaguchi H, Kohzai A, Hatakeyama K, Fujine S, Yoneda K, Kanda K and Esaka T 2000 Visualization of hydrogen in hydrogen storage alloys using neutron radiography *Int. J. Hydrogen Energy* **25** 1205

[73] 2007 Own unpublished results

[74] Schillinger B, Abele H, Brunner J, Frei G, Gähler R, Gildemeister A, Hillenbach A, Lehmann E and Vontobel P 2005 Detection systems for short-time stroboscopic neutron imaging and measurements on a rotating engine *Nucl. Instrum. Methods Phys. Res.* A **542** 142

[75] Brunner J, Lehmann E and Schillinger B 2005 Dynamic neutron radiography of a combustion engine *Proc. 7th World Conf. on Neutron Radiography (WCNR-7, Rome, Italy, 2005)* ed P Chirco and R Rosa (Rome: ENEA)

[76] Ferger T, Abele H, Brunner J, Gaehler R, Schillinger B and Villard J R 2005 The new station for fast radiography and tomography at the ILL in Grenoble *Proc. 7th World Conf. on Neutron Radiography (WCNR-7, Rome, Italy, 2005)* ed P Chirco and R Rosa (Rome: ENEA)

[77] Hillenbach A, Engelhardt M, Abele H and Gähler R 2005 High flux neutron imaging for high-speed tomography, dynamic tomography and strongly absorbing materials *Nucl. Instrum. Methods Phys. Res.* A **542** 116

[78] Dierick M, Vlassenbroeck J, Masschaele B, Cnudde V, Van Hoorebeke L and Hillenbach A 2005 High-speed neutron tomography of dynamic processes *Nucl. Instrum. Methods Phys. Res.* A **542** 296

[79] Schillinger B, Brunner J and Calzada E 2006 A study of oil lubrication in a rotating engine using stroboscopic neutron imaging *Physica* B **385–386** 921

[80] Matsushima U, Kardjilov N, Hilger A, Ueno M, Kawamitsu Y, Nishizawa T and Herppich W B 2008 Visualisation of water flow in tomato seedlings using neutron imaging *Proc. 8th World Conf. on Neutron Radiography (WCNR-8, Gaithersburg, USA, 2006)* ed M Arif and R G Downing (Lancaster, PA: DESTech Publ. Inc.)

[81] Oswald S E, Menon M, Carminati A, Vontobel P, Lehmann E and Schulin R 2008 Quantitative imaging of infiltration, root growth, and root water uptake via neutron radiography *Vadose Zone J.* **7** 1035

[82] Lehmann E, Hartmann S and Wyer P 2005 Neutron radiography as visualization and quantification method for conservation measures of wood firmness enhancement *Nucl. Instrum. Methods Phys. Res.* A **542** 68

[83] Manescu A, Fiori F, Giuliani A, Kardjilov N, Kasztovszky Z, Rustichelli F and Straumal B 2008 Non-destructive compositional analysis of historic organ reed pipes *J. Phys.: Condens. Matter* **20** 104250

[84] Festa G, Caroppi P A, Filabozzi A, Andreani C, Arancio M L, Triolo R, Celso F Lo, Benfante V and Imberti S 2008 Composition and corrosion phases of Etruscan Bronzes from Villanovan Age *Meas. Sci. Technol.* **19** 034004

[85] Kardjilov N, Hilger A, Manke I, Benfante V, Lo Celso F, Triolo R, Ruffo I and Tusa S 2008 Neutron tomography in modern archaeology *Not. Neutroni Luce Sincrotrone* **13** 6

[86] Rant J J, Milič Z, Turk P and Lengar I 2005 Neutron radiography as a NDT method in archeology *Proc. 8th Int. Conf. Slovenian Society for Non-Destructive Testing (Portorož, Slovenia, 2005)* (Ljubljana, Slovenia: Slovenian Society of Non-destructive Testing) p 181

[87] Strobl M 2003 New alternative contrast methods in neutron computer tomography *PhD Thesis* TU Wien

[88] Strobl M, Treimer W and Hilger A 2006 Scattering-related contrast signals in neutron computerized tomography and the new V12 instrument at HMI Berlin *Physica* B **385–386** 1209

[89] Strobl M, Treimer W, Ritzoulis C, Wagh A G, Abbas S and Manke I 2007 The new V12 ultra-small-angle neutron scattering and tomography instrument at the Hahn-Meitner Institute *J. Appl. Crystallogr.* **40** 463

[90] Kockelmann W, Frei G, Lehmann E, Vontobel P and Santisteban J R 2007 Energy selective transmission imaging at a pulsed source *Nucl. Instrum. Methods Phys. Res.* A **578** 421

[91] Kardjilov N 2003 Further developments and applications of radiography and tomography with thermal and cold neutrons *PhD Thesis* TU München

[92] Kardjilov N, Baechler S, Bastuerk M and Dierick M 2003 New features in cold neutron radiography and tomography: II. Applied energy-selective neutron radiography and tomography *Nucl. Instrum. Methods Phys. Res.* A **501** 536

[93] Treimer W, Strobl M, Hilger A, Kardjilov N and Manke I 2006 A wavelength tunable device for neutron radiography and tomography *Appl. Phys. Lett.* **89** 203504

[94] Schulz M, Böni P, Calzada E, Mühlbauer M and Schillinger B 2009 Energy-dependent neutron imaging with a double crystal monochromator at the ANTARES facility at FRMII *Nucl. Instrum. Methods Phys. Res.* A **605** 33

[95] Tamaki M 2005 Conceptual monochromatic digital neutron radiography using continuous cold neutron beam *Nucl. Instrum. Methods Phys. Res.* A **542** 32

[96] Strobl M, Treimer W, Kardjilov N and Hilger A 2005 Application of refraction contrast tomography *Nucl. Instrum. Methods Phys. Res.* A **542** 383

[97] Kardjilov N, de Beer F, Hassanein R, Lehmann E and Vontobel P 2005 Scattering corrections in neutron radiography using point scattered functions *Nucl. Instrum. Methods Phys. Res.* A **542** 336

[98] Hassanein R, de Beer F, Kardjilov N and Lehmann E 2006 Scattering correction algorithm for neutron radiography and tomography tested at facilities with different beam characteristics *Physica* B **385–386** 1194

[99] Kardjilov N, Lehmann E and Vontobel P 2002 Representation of the image formation in applied neutron radiography in terms of a PSF superposition *Appl. Phys.* A **74** 228

[100] Strobl M 2009 Future prospects of imaging at spallation neutron sources *Nucl. Instrum. Methods Phys. Res.* A **604** 646

[101] Dubus F, Bonse U, Zawisky M, Baron M and Loidl R 2005 First phase-contrast tomography with thermal neutrons *IEEE Trans. Nucl. Sci.* **52** 364

[102] Zawisky M, Bonse U, Dubus F, Hradil Z and Řeháček J 2004 Neutron phase contrast tomography on isotope mixtures *Europhys. Lett.* **68** 337

[103] Podurets K M,Somenkov V A and Shil'shtein S Sh 1989 Neutron radiography with refraction contrast *Physica* B **156–157** 691

[104] Hainbuchner M, Villa M, Kroupa G, Bruckner G, Baron M, Amenitsch H, Seidl E and Rauch H 2000 The new high resolution ultra small-angle neutron scattering instrument at the High Flux Reactor in Grenoble *J. Appl. Crystallogr.* **33** 851

[105] Treimer W, Strobl M, Hilger A, Seifert C and Feye-Treimer U 2003 Refraction as imaging signal for computerized (neutron) tomography *Appl. Phys. Lett.* **83** 398

[106] Strobl M, Treimer W and Hilger A 2004 Small angle scattering signals for (neutron) computerized tomography *Appl. Phys. Lett.* **85** 488

[107] Strobl M, Treimer W and Hilger A 2004 First realisation of a three-dimensional refraction contrast computerised neutron tomography *Nucl. Instrum. Methods Phys. Res.* B **222** 653

[108] Allman B E, McMahon P J, Nugent K A, Paganin D, Jacobson D L, Arif M and Werner S A 2000 Phase radiography with neutrons *Nature* **408** 158

[109] McMahon P J, Allman B E, Jacobson D L, Arif M, Werner S A and Nugent K A 2003 Quantitative phase radiography with polychromatic neutrons *Phys. Rev. Lett.* **91** 145502

[110] Kardjilov N, Lehmann E, Steichele E and Vontobel P 2004 Phase-contrast radiography with a polychromatic neutron beam *Nucl. Instrum. Methods Phys. Res.* A **527** 519

[111] Jacobson D L, Allman B E, McMahon P J, Nugent K A, Paganin D, Arif M and Werner S A 2004 Thermal and cold neutron phase-contrast radiography *Appl. Radiat. Isot.* **61** 547

[112] Strobl M, Treimer W, Kardjilov N, Hilger A and Zabler S 2008 On neutron phase contrast imaging *Nucl. Instrum. Methods Phys. Res.* **266** 181

[113] Kardjilov N, Lee S W, Lehmann E, Lim I C, Sim C M and Vontobel P 2005 Improving the image contrast and resolution in the phase-contrast neutron radiography *Nucl. Instrum. Methods Phys. Res.* A **542** 100

[114] Lehmann E, Lorenz K, Steichele E and Vontobel P 2005 Non-destructive testing with neutron phase contrast imaging *Nucl. Instrum. Methods Phys. Res.* A **542** 95

[115] Pfeiffer F, Weitkamp T, Bunk O and David C 2006 Phase retrieval and differential phase-contrast imaging with low-brilliance X-ray sources *Nature Phys.* **2** 258
[116] Pfeiffer F, Grümzweig C, Bunk O, Frei G, Lehmann E and David C 2006 Neutron phase imaging and tomography *Phys. Rev. Lett.* **96** 215505
[117] Strobl M, Staack K, Treimer W and Hilger A 2008 Quantitative neutron phase contrast tomography *Meas. Sci. Technol.* **19** 034020
[118] Morrison G R and Browne M T 1992 Dark-field imaging with the scanning transmission x-ray microscope *Rev. Sci. Instrum.* **63** 611
[119] Strobl M, Grünzweig C, Hilger A, Manke I, Kardjilov N, David C and Pfeiffer F 2008 Neutron dark-field tomography *Phys. Rev. Lett.* **101** 123902
[120] Badurek G, Hochhold M and Leeb H 1997 Neutron magnetic tomography—a novel technique *Physica* B **234–236** 1171
[121] Jericha E, Szeywerth R, Leeb H and Badurek G 2008 Perfect crystal neutron interferometry and tensorial neutron tomography *Nucl. Instrum. Methods Phys. Res.* A **586** 119
[122] Leeb H, Szeywerth R, Jericha E and Badurek G 2005 Towards manageable magnetic field retrieval in bulk materials *Physica* B **356** 187
[123] Jericha E, Szeywerth R, Leeb H and Badurek G 2007 Reconstruction techniques for tensorial neutron tomography *Physica* B **397** 159
[124] Treimer W, Hilger A, Kardjilov N and Strobl M 2005 Review about old and new imaging signals for neutron computerized tomography *Nucl. Instrum. Methods Phys. Res.* A **542** 367
[125] Kardjilov N, Manke I, Strobl M, Hilger A, Treimer W, Meissner M, Krist T and Banhart J 2008 Three-dimensional imaging of magnetic fields with polarized neutrons *Nature Phys.* **4** 399
[126] Schulz M 2008 *Conference contribution at ITMNR-6 (Kobe, Japan, 2008)*
[127] Tasaki S 2008 *Conference contribution at PNCMI (Tokai, Japan, 2008)*
[128] Kageyama M, Tasaki S, Hino M, Ebisawa T, Yamazaki D, Hayashida H and Abe Y 2009 Development of neutron spin phase contrast imaging *Physica* B **404** 2615
[129] Piegsa F M, van den Brandt B, Hautle P and Konter J A 2008 Neutron spin phase imaging *Nucl. Instrum. Methods Phys. Res.* A **586** 15
[130] Schulz M, Böni P, Calzada E, Mühlbauer M, Neubauer A and Schillinger 2009 A polarizing neutron periscope for neutron imaging *Nucl. Instrum. Methods Phys. Res.* A **605** 43
[131] Schlenker M, Bauspiess W, Graeff W, Bonse U and Rauch H 1980 Imaging of ferromagnetic domains by neutron interferometry *J. Magn. Magn. Mater.* **15–8** 1507
[132] Strobl M, Treimer W, Walter P, Keil S and Manke I 2007 Magnetic field induced differential neutron phase contrast imaging *Appl. Phys. Lett.* **91** 254104
[133] Strobl M, Hilger A, Kardjilov N, Ebrahimi O, Keil S and Manke I 2009 Differential phase contrast and dark field neutron imaging *Nucl. Instrum. Methods Phys. Res.* A **605** 9
[134] Podurets K M, Chistyakov R R and Shil'shtein S Sh 1994 Observation of the magnetization process of a thick ferromagnet by neutron radiography with refraction-produced contrast *Zh. Tekh. Fiz.* **67** 134
[135] Grünzweig C, David C, Bunk O, Dierolf M, Frei G, Kühne G, Schäfer R, Pofahl S, Rønnow H M R and Pfeiffer F 2008 Bulk magnetic domain structures visualized by neutron dark-field imaging *Appl. Phys. Lett.* **93** 112504